5-27-2007

Influence of lateral and top boundary conditions on regional air quality prediction: A multiscale study coupling regional and global chemical transport models

Youhua Tang
University of Iowa

Gregory R. Carmichael
University of Iowa

Narisara Thongbongchoo
King Mongkut's Institute of Technology

Tianfeng Chai
University of Iowa

Larry Horowitz
NOAA

See next page for additional authors

Recommended Citation

Tang, Y., et al. (2007), Influence of lateral and top boundary conditions on regional air quality prediction: A multiscale study coupling regional and global chemical transport models, J. Geophys. Res., 112, D10S18, doi:10.1029/2006JD007515.

Influence of lateral and top boundary conditions on regional air quality prediction: A multiscale study coupling regional and global chemical transport models

Youhua Tang,[1,2] Gregory R. Carmichael,[1] Narisara Thongboonchoo,[1] Tianfeng Chai,[1] Larry W. Horowitz,[3] Robert B. Pierce,[4] Jassim A. Al-Saadi,[4] Gabriele Pfister,[5] Jeffrey M. Vukovich,[6] Melody A. Avery,[4] Glen W. Sachse,[4] Thomas B. Ryerson,[7] John S. Holloway,[7] Elliot L. Atlas,[8] Frank M. Flocke,[5] Rodney J. Weber,[9] L. Gregory Huey,[9] Jack E. Dibb,[10] David G. Streets,[11] and William H. Brune[12]

Received 16 May 2006; revised 27 November 2006; accepted 8 January 2007; published 25 April 2007.

[1] The sensitivity of regional air quality model to various lateral and top boundary conditions is studied at 2 scales: a 60 km domain covering the whole USA and a 12 km domain over northeastern USA. Three global models (MOZART-NCAR, MOZART-GFDL and RAQMS) are used to drive the STEM-2K3 regional model with time-varied lateral and top boundary conditions (BCs). The regional simulations with different global BCs are examined using ICARTT aircraft measurements performed in the summer of 2004, and the simulations are shown to be sensitive to the boundary conditions from the global models, especially for relatively long-lived species, like CO and O_3. Differences in the mean CO concentrations from three different global-model boundary conditions are as large as 40 ppbv, and the effects of the BCs on CO are shown to be important throughout the troposphere, even near surface. Top boundary conditions show strong effect on O_3 predictions above 4 km. Over certain model grids, the model's sensitivity to BCs is found to depend not only on the distance from the domain's top and lateral boundaries, downwind/upwind situation, but also on regional emissions and species properties. The near-surface prediction over polluted area is usually not as sensitive to the variation of BCs, but to the magnitude of their background concentrations. We also test the sensitivity of model to temporal and spatial variations of the BCs by comparing the simulations with time-varied BCs to the corresponding simulations with time-mean and profile BCs. Removing the time variation of BCs leads to a significant bias on the variation prediction and sometime causes the bias in predicted mean values. The effect of model resolution on the BC sensitivity is also studied.

Citation: Tang, Y., et al. (2007), Influence of lateral and top boundary conditions on regional air quality prediction: A multiscale study coupling regional and global chemical transport models, *J. Geophys. Res.*, *112*, D10S18, doi:10.1029/2006JD007515.

1. Introduction

[2] Lateral and top boundary conditions (BCs) are a major uncertain factor in regional air quality prediction. Mesoscale meteorological models, like MM5, RAMS and WRF, usually use lateral boundary conditions supplied by global meteorological models. In principle, regional chemical transport/air quality model should also import boundary conditions from corresponding global models in order to consider the external forcings. However, additional uncertainties are introduced in this importing process because of the uncertainties in the global models, and because of differences in resolution between the global and regional

[1]Center for Global and Regional Environmental Research, University of Iowa, Iowa City, Iowa, USA.
[2]Now at Environmental Modeling Center, National Centers for Environmental Prediction, NOAA, Camp Springs, Maryland, USA.
[3]Geophysical Fluid Dynamics Laboratory, NOAA, Princeton, New Jersey, USA.
[4]NASA Langley Research Center, Hampton, Virginia, USA.
[5]National Center for Atmospheric Research, Boulder, Colorado, USA.
[6]Carolina Environmental Program, University of North Carolina, Chapel Hill, North Carolina, USA.
[7]Chemical Sciences Division, Earth System Research Laboratory, NOAA, Boulder, Colorado, USA.
[8]Rosenstiel School of Marine and Atmospheric Science, University of Miami, Miami, Florida, USA.
[9]School of Earth and Atmospheric Sciences, Georgia Institute of Technology, Atlanta, Georgia, USA.
[10]Institute for the Study of Earth, Oceans, and Space, University of New Hampshire, Durham, New Hampshire, USA.
[11]Argonne National Laboratory, Argonne, Illinois, USA.
[12]Department of Meteorology, Pennsylvania State University, University Park, Pennsylvania, USA.

0148-0227/07/2006JD007515

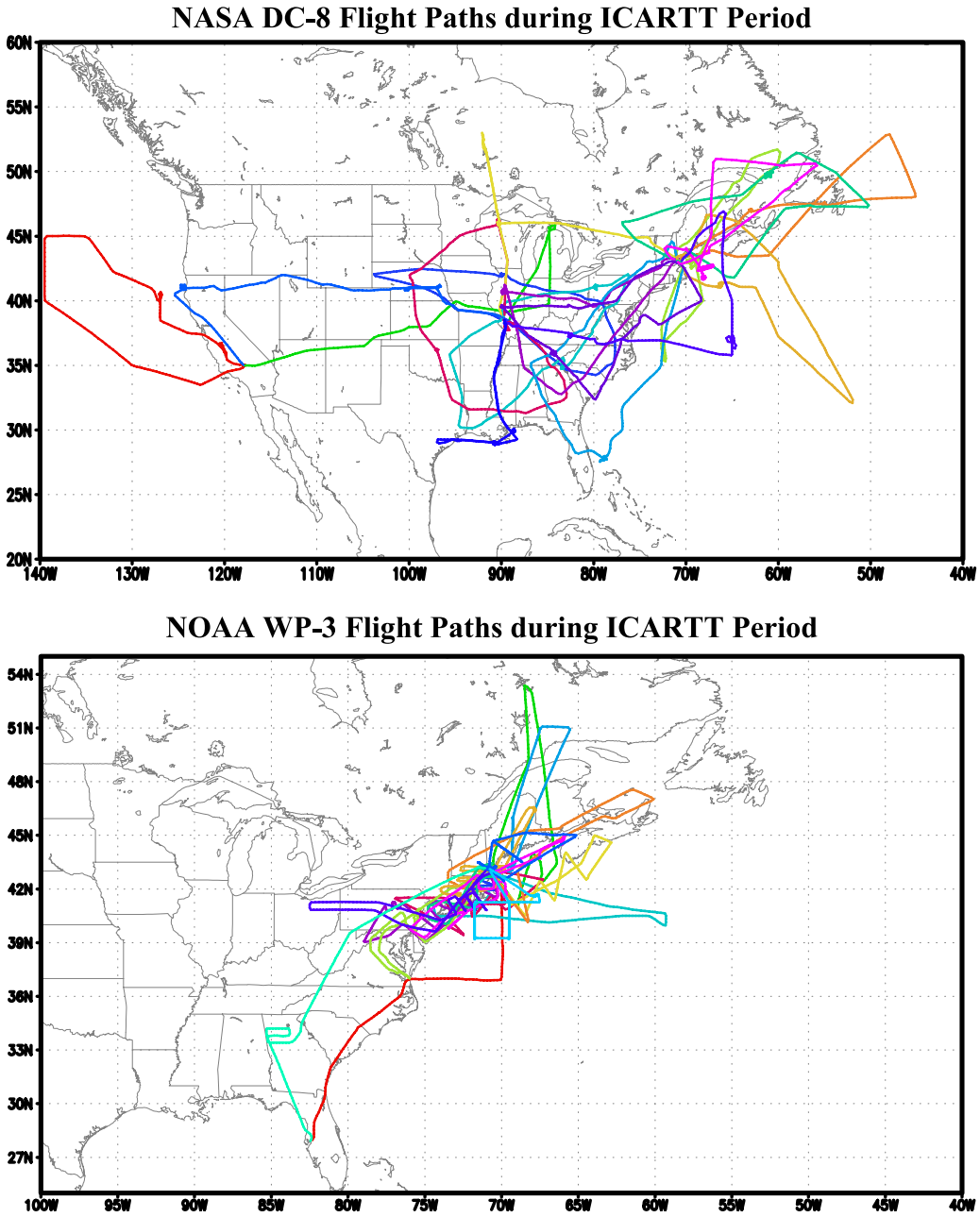

Figure 1. DC-8 and WP-3 flight paths during the ICARTT period. The colors show different flights.

models, and differences in model formations, such as chemical mechanisms. In the past, most regional chemical transport models have used fixed concentration profiles as their boundary conditions. These concentration profiles should represent the mean concentrations during the period of interest. Some profiles are based on historical measurements [*Winner et al.*, 1995], and some profiles are set to typical clean concentrations [*Chen et al.*, 2003]. Typically the profile boundary conditions lack temporal and spatial variations, and thus the corresponding specific variability in the regional simulation mainly reflects the contributions of emissions, transport and chemical processes within the model domain.

[3] The ICARTT (International Consortium for Atmospheric Research on Transport and Transformation) field experiment was performed in the summer of 2004 (http://www.esrl.noaa.gov/csd/ICARTT/), and included NASA INTEX-A (Intercontinental Chemical Transport Experiment–A), the NOAA NEAQS/ITCT-2k4 (New England Air Quality Study–Intercontinental Transport and Chemical Transformation, 2004), and other coordinated studies. During the ICARTT period, the NASA DC-8 aircraft performed 18 research flights covering the continental USA, and the NOAA WP-3 aircraft had 18 research flights, mainly over northeastern USA (Figure 1). Some of these flights encountered remote signatures, such as Asian air masses, long-range transported biomass burning plumes, and stratospheric air mass intrusions. Tropospheric regional chemical transport model cannot predict these phenomena without appropriate lateral and top boundary conditions. The ICARTT

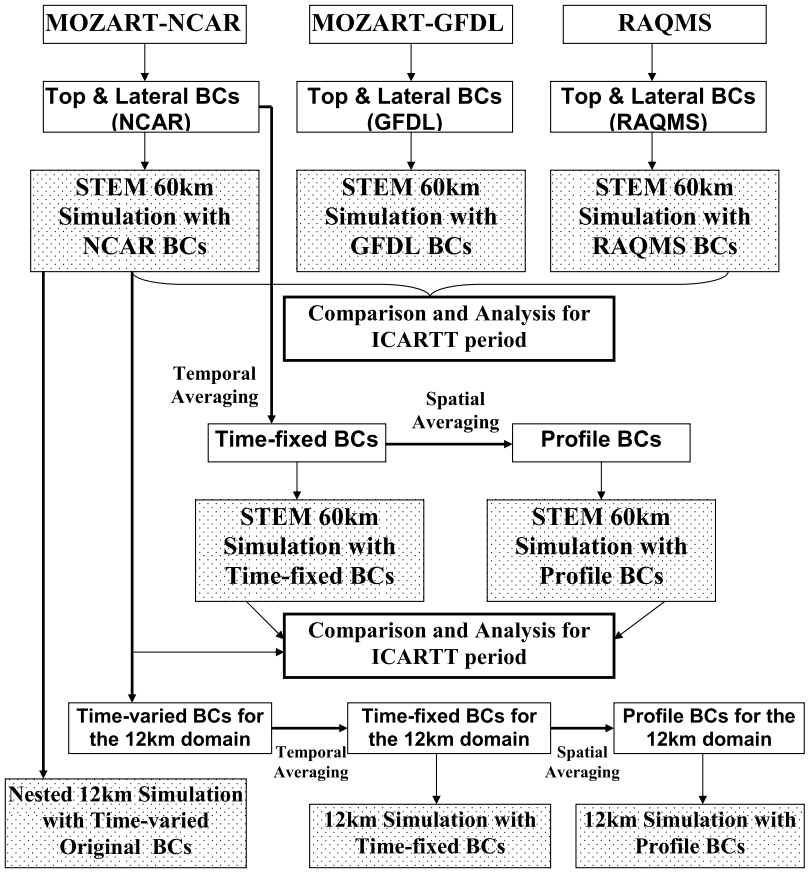

Figure 2. Comparison and analysis framework.

airborne measurements provide an opportunity to examine the performance of a regional model driven by different boundary conditions from different global models. We can also test the dependence of regional model on the BCs under different spatial and temporal scales.

[4] In this study we evaluate the sensitivity and performance of regional model predictions to various BC treatments. We specifically employed the regional chemical transport model STEM-2K3 [*Tang et al.*, 2004] with lateral and top boundary conditions from three global models: MOZART-NCAR, MOZART-GFDL and RAQMS. Figure 2 shows the framework of this study. First, we compare regional model predictions driven by the BCs from three different global models, and evaluate the variations in regional predictions caused by the BCs. Next, we perform study for the model sensitivity to the temporal and spatial variations of BCs by comparing model predictions with the original time-varied BCs to simulations with temporal and spatial averaged BCs. The sensitivity study is performed in two domains: a 60 km primary domain covering continental USA and a 12 km nested domain over the northeastern USA. Finally we discuss the implications of these results for improving regional air quality predictions.

2. Methodology

[5] We employ the STEM-2K3 [*Tang et al.*, 2004] regional chemical transport model, which is a flexible regional-scale chemical transport model. In this study, SAPRC99 chemical mechanism [*Carter*, 2000] with online photolysis solver [*Tang et al.*, 2003] and SCAPE II (Simulating Composition of Atmospheric Particles at Equilibrium) [*Kim et al.*, 1993a, 1993b; *Kim and Seinfeld*, 1995] aerosol module were used. MM5 meteorological model driven by NCEP FNL (Final Global Data Assimilation System) $1^\circ \times 1^\circ$ analyzed data every 6 hours was used for the meteorological fields. The STEM model used the same grid system as MM5. The MM5 simulations were performed in a 60 km domain covering North America (Figure 3), and a one-way nested 12 km domain that covered the northeastern USA, with sigma layers extending from surface to 100 hPa: 0.999, 0.9965, 0.9925, 0.985, 0.97, 0.945, 0.91, 0.87, 0.825, 0.77, 0.71, 0.65, 0.59, 0.53, 0.47, 0.41, 0.35, 0.285, 0.21, 0.125, and 0.04. Grid nudging was performed every 6 hours, and reinitialization with FNL data took place every 72 hours. The cloud scheme of *Grell et al.* [1994] was chosen for the physical parameterization, and the MRF scheme [*Hong and Pan*, 1996] was employed for PBL parameterization.

2.1. Emissions

[6] During the ICARTT field experiment the U.S. EPA National Emission Inventory (NEI) with base year 1999 was used for forecasting. In this study, the NEI-2001 version 3 emission was employed. It should be noted that NEI-2001 and NEI-1999 emissions differ significantly in CO, NO_x and SO_2, and the difference between the forecast and post

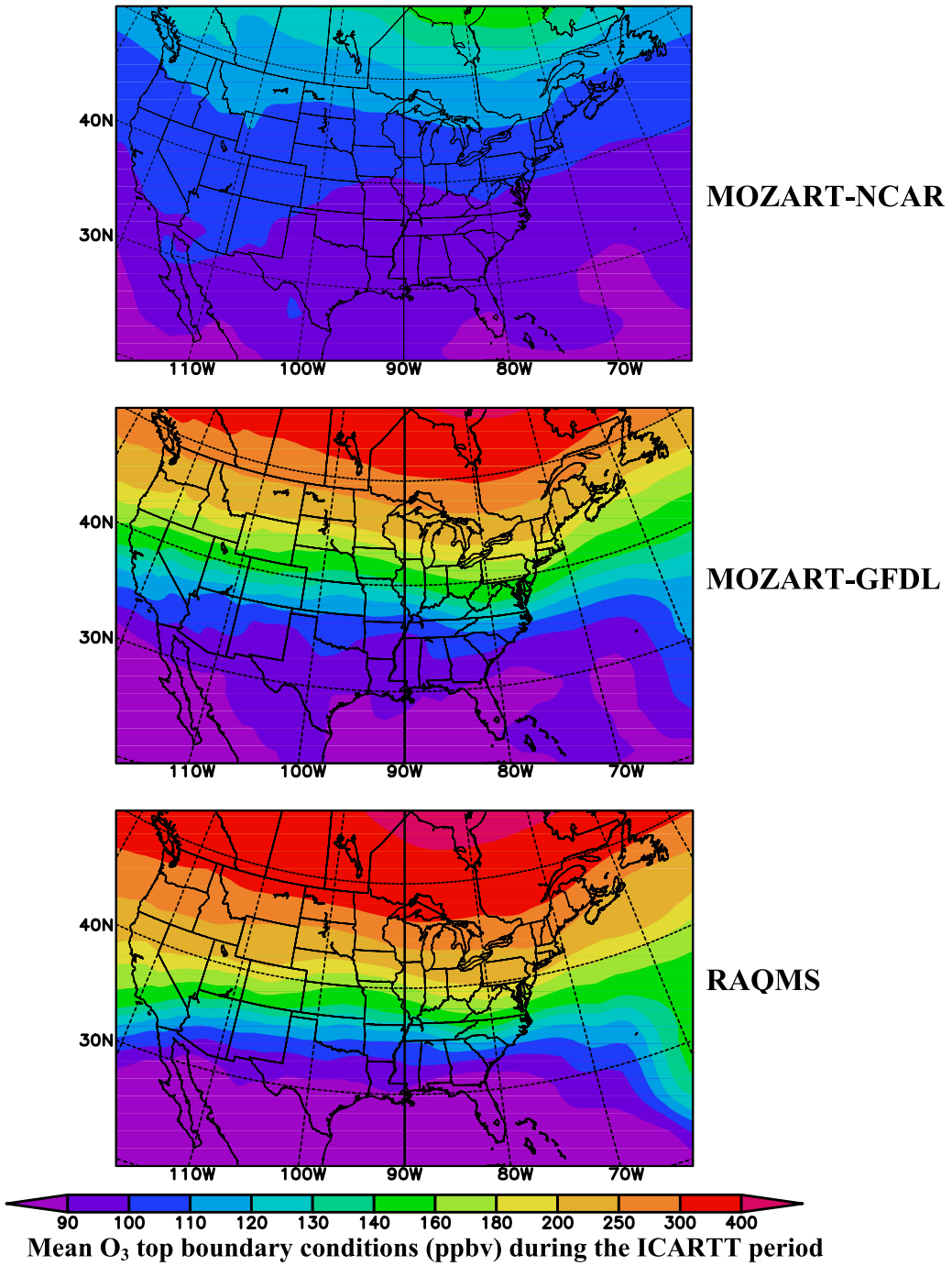

Figure 3. Period-mean O_3 top boundary conditions from three global models.

simulation reflect these emission differences. To reflect systematic differences between the observations and predictions, we adjusted the NEI-2001v3 VOC emissions; light alkanes (ethane and propane) were doubled, and aromatic emissions were reduced by 30%. The NEI-2001 version 3 inventory still tends to overestimate NO_x emission when we apply it to this simulation for summer 2004, as it did not consider the substantial NO_x reductions in the 2004 utility emissions, such as that documented by *Frost et al.* [2006]. In this study, we also included aviation emissions from the EDGAR emission inventory [*Olivier and Berdowski*, 2001].

[7] Lightning NO_x emissions were explicitly treated in this study using data from National Lightning Detection Network (NLDN). NLDN data includes hourly lightning location, signal strength and multiplicity in strokes/flash. We used the method of *Price and Penner* [1997] to derive the lightning NO_x emissions, and we used MM5's meteorological information (cloud water content and temperature) to identify the existence of cloud, cloud top and cloud freezing level [*Pickering et al.*, 1998]. Both cloud-to-ground (CG) and intracloud (IC) flashes were treated and contributed to the NO_x source. The IC/CG ratio is an important

Table 1. Three Global Models and Their Configurations Used in ICARTT

	MOZART-NCAR	MOZART-GFDL	RAQMS
Horizontal resolution	2.8° × 2.8°	1.89° × 1.89°	1.4° × 1.4°
Meteorology	NCEP reanalysis	NCEP reanalysis	GFS analysis
Anthropogenic emissions	*Granier et al.* [2004]	EDGAR Version 2 (1990) [*Olivier and Berdowski*, 2001]	GEIA/EDGAR inventory with updated Asian emission [*Streets et al.*, 2003]
Biomass burning emissions	MOPITT derived [*Pfister et al.*, 2005]	*Turquety et al.* [2007]	climatological data
stratospheric ozone	synthetic ozone constrain [*McLinden et al.*, 2000]	relaxed to climatology [*Horowitz et al.*, 2003]	TOMS column assimilation [*Pierce et al.*, 2007]

factor. Here we adopted the methods of *Pickering et al.* [1998] and *Price and Penner* [1997] to calculating the lightning NO_x emissions. In the vertical direction, CG lightning NO_x was uniformly distributed from cloud top to ground. The breakthrough potential of the intracloud lightning was set at 1/10 of the CG lightning [*Price and Penner*, 1997]. We set the negative CG lightning NO_x producing rate to 1×10^{17} molecules/J and the positive CG to a value of 1.6 times of this value [*Price and Penner*, 1997].

[8] The biogenic emission inventory system 2 (BEIS 2) [*Geron et al.*, 1994] was used to generate time-varied isoprene and monoterpene emissions driven by the MM5 meteorological fields. During the ICARTT period, forest fires occurred in Alaska and northwestern Canada, which was out of the regional model domain. However, the lateral boundary conditions from global models provided the time-varied biomass burning CO and other species.

[9] Sea salt emissions were estimated using the *Gong* [2003] method driven by MM5's 10 m wind speed. In this study, size-resolved sea salt emissions enter 4 aerosol size bins (in diameter): 0.1–0.3 μm, 0.3–1.0 μm, 1.0–2.5 μm, and 2.5–10 μm [*Tang et al.*, 2004].

[10] The evaluations for the performance of the STEM predictions are presented elsewhere (M. Mena-Carrasco et al., Improving regional ozone modeling through systematic evaluation of errors using the aircraft observations during ICARTT, submitted to *Journal of Geophysical Research,* 2006). In this study, we focus on the influence of the boundary-condition difference on model predictions.

2.2. Top and Lateral Boundary Conditions

[11] In this study, lateral and top boundary conditions from three global models: the MOZART-NCAR (National Center for Atmospheric Research); the MOZART-GFDL (NOAA GFDL laboratory); and the RAQMS (NASA Langley Research Center). These models produced different regional BCs, which reflect differences in emissions, meteorology, chemical mechanism and treatments of stratospheric ozone and exchanges between the global models. Table 1 shows the three global models that provide BCs for this study. These two MOZART (Model for Ozone and Related chemical Tracers) [*Horowitz et al.*, 2003] simulations used different configurations: MOZART-NCAR was run by Gabriele Pfister with a 2.8° horizontal resolution and MOPITT satellite derived forest fire emissions [*Pfister et al.*, 2005], biofuel and fossil fuel emissions of *Granier et al.* [2004], and NCEP reanalysis meteorology. In contrast MOZART-GFDL was run by Larry Horowitz with a 1.89° horizontal resolution, NCEP reanalysis meteorology, stratospheric O_3 relaxed to climatology, EDGAR Version 2 (1990) [*Olivier and Berdowski*, 2001] fossil fuel emissions, and forest fire emissions estimated by Harvard University [*Turquety et al.*, 2007]. RAQMS (Real-time Air Quality Modeling System) is a multiscale chemical transport model that can run either globally or regionally [*Pierce et al.*, 2003]. During the ICARTT period, RAQMS was run globally at 1.4° horizontal resolution with meteorological fields initialized from the NOAA GFS analysis every 6 hours, and included stratospheric ozone profile assimilation in addition to the TOMS column assimilation [*Pierce et al.*, 2007]. RAQMS uses climatological emissions for NO_x and CO from GEIA/EDGAR inventory with updated Asian emissions from *Streets et al.* [2003], biogenic CO from *Duncan and Bey* [2004] and aircraft NO_x emission from HSRP database [*Stolarski et al.*, 1995]. Each global model was used in the analysis of the ICARTT observations, and the further details about the individual models and their differences are given by *Pfister et al.* [2005], *Horowitz et al.* [2003] and *Pierce et al.* [2007].

[12] In this study, we imported time-dependent top and lateral boundary conditions for STEM-2K3 from the three global models in every 6 hours. Figure 3 shows the mean O_3 top boundary conditions from the three global models used by STEM. STEM's top is the same as the top of MM5, or 100 hPa in MM5's reference atmosphere. Figure 3 also shows the STEM primary domain: 97 × 62 grids in 60 km horizontal resolution. As shown in Figure 3, RAQMS provided the highest O_3 top boundary, and MOZART-GFDL had an ozone boundary condition similar to RAQMS but about 10% lower. The MOZART-NCAR's top boundary is significantly lower than the other two models by up to 100–200 ppbv, especially north of 40°N. MOZART-NCAR uses a synthetic ozone ("SYNOZ") representation [*McLinden et al.*, 2000] in order to constrain the stratospheric flux of ozone [*Emmons et al.*, 2007]. *Horowitz et al.* [2007] found that the O_3 predictions by MOZART-GFDL were lower (−10 ppbv) than ICARTT aircraft measurements in middle to upper troposphere. RAQMS predictions were shown to overpredict O_3 in the upper troposphere/lower stratosphere [*Pierce et al.*, 2007].

[13] Figure 4 shows the corresponding CO lateral boundary conditions from the global models. RAQMS tends to yield 20–40 ppbv lower CO concentrations than the two MOZART models in the south and east boundaries of the STEM 60 km domain. Among these three lateral boundary conditions, MOZART-GFDL produced the highest mean CO concentrations, and the highest CO west boundary condition, which is the major inflow boundary. All of these models have relatively high CO concentrations along the

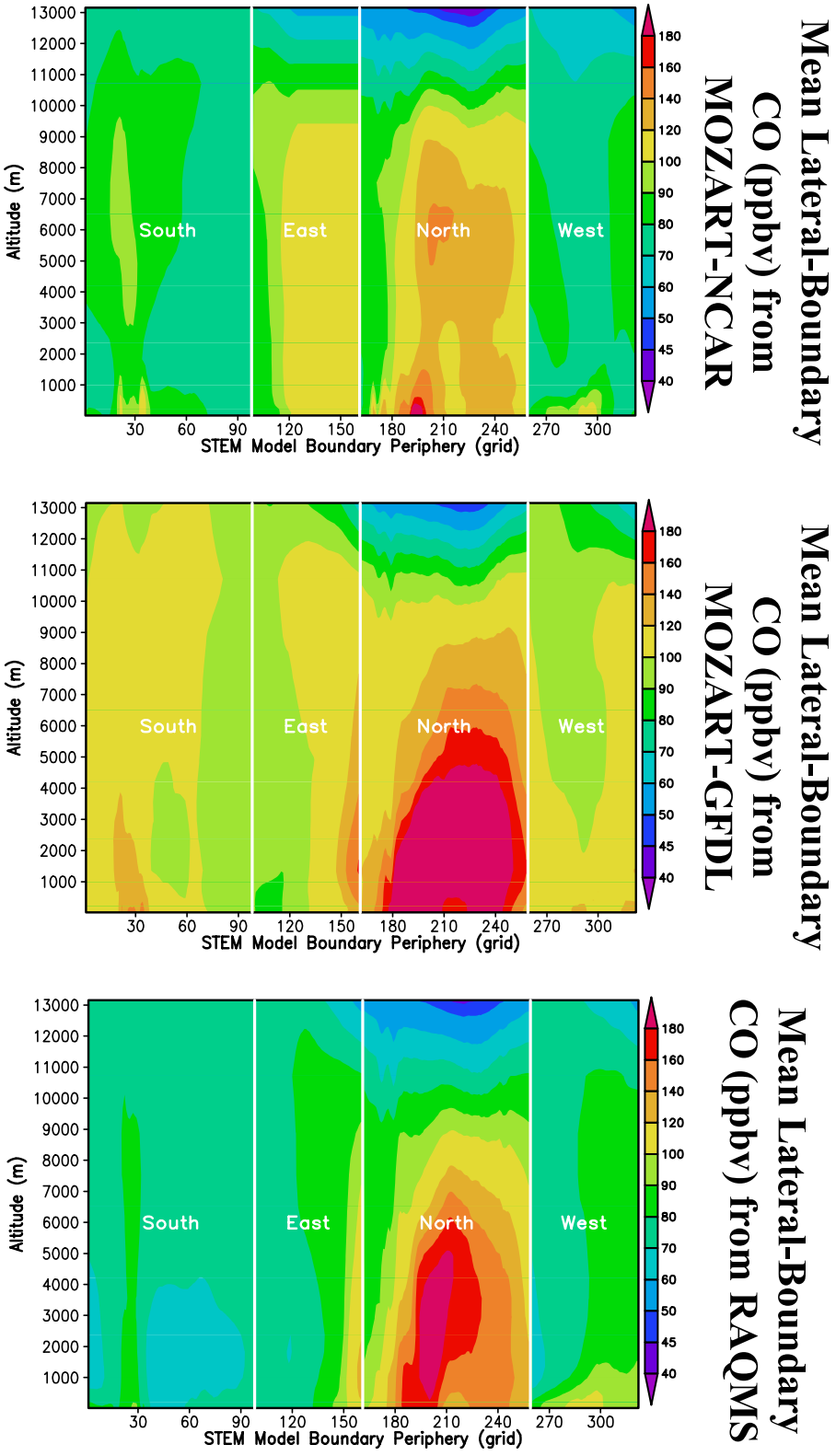

Figure 4. Period-mean CO lateral boundary conditions from three global models, along the STEM's boundary periphery in grid (60 km) starting from the southwest corner of the STEM 60 km domain shown in Figure 3.

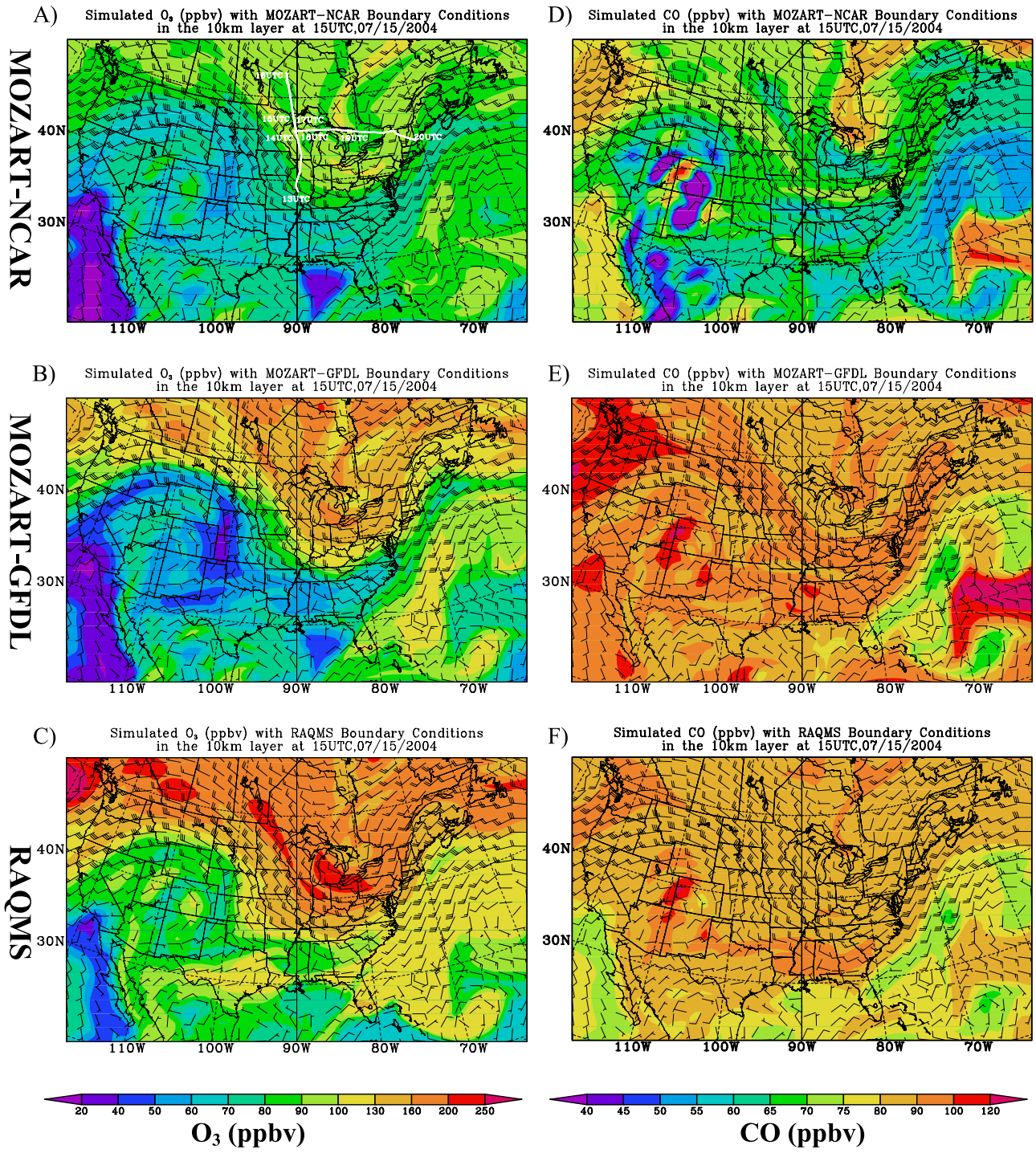

Figure 5. STEM 60 km simulated O_3 and CO concentrations at 1500 UTC, in the 10 km layer with boundary conditions from the three global models for DC-8 flight 8 on 15 July: (a) simulated O_3 with MOZART-NCAR BCs (shows the flight path), (b) simulated O_3 with MOZART-GFDL BCs, (c) simulated O_3 with RAQMS BCs, (d) simulated CO with MOZART-NCAR BCs, (e) simulated CO with MOZART-GFDL BCs, and (f) simulated CO with RAQMS BCs.

north boundary condition, which reflect the forest fire emissions in Alaska and Canada. MOZART-GFDL has the highest biomass burning CO concentration among these 3 models, and this high CO concentration extends from the surface to about 6 km. RAQMS's mean CO concentration in the north boundary is similar to MOZART-GFDL, but has a relatively narrow high-CO plume. MOZART-NCAR shows an isolated CO hot spot at the altitude of 7 km. These

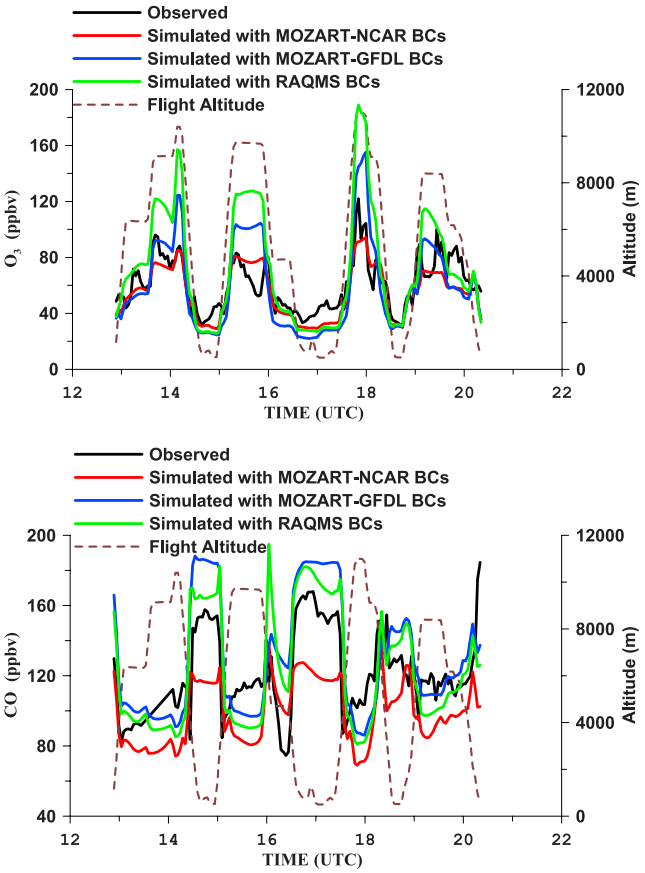

Figure 6. Observed and simulated O_3 and CO concentrations for the DC-8 flight 8 on 15 July 2004.

differences reflect their different emission inventories, and different release heights of the biomass burning sources.

[14] It should also be emphasized that both Figures 3 and 4 illustrate the period-mean boundary conditions from the three global models. The regional simulations used time-varied BCs, for which differences between the differences between BCs for certain periods could be much greater than those discussed above.

2.3. Analysis Method for the Sensitivity to Boundary Conditions

[15] First, simulations were performed using spatial and temporal varying BCs from the global models and results from these simulations are compared to the ICARTT flight observations. We examined the regional model's sensitivity to temporal and spatial variations of BCs as outlined in Figure 2. In addition, by averaging the boundary conditions inputs spatially and temporally, we can remove the temporal and spatial variations in the BCs. Simulations with temporally and spatially averaging BCs were performed to evaluate the sensitivity of the regional prediction to the temporal and spatial variations of BCs. These studies were performed for 60 km and 12 km domains, respectively.

3. Effect of Different Boundary Conditions

[16] We performed three STEM regional simulations driven by the three different sets of boundary conditions, and compared these simulations with aircraft measurements for the ICARTT period. All the STEM regional simulations used the same emission and settings except for their top and lateral boundary conditions. At first, we present results for one ICARTT flight to illustrate the sensitivity of the regional predictions to the BCs. The DC-8 flight 8 was a transit research flight from St. Louis to New Hampshire. This flight encountered a concentrated plume transported from the northwest boundary at around 1600 UTC.

[17] Figure 5 shows the DC-8 flight path (Figure 5a) along with the O_3 and CO horizontal distributions at 10 km predicted with the three BCs at 1500 UTC. Figure 6 shows the comparison of CO and O_3 between the observations and the simulations. All these simulations captured similar general features to those observed. The STEM simulations with MOZART-GFDL and RAQMS BCs tend to have higher O_3 concentrations than observed for altitudes >6 km, and the simulation with MOZART-NCAR produced values closest to the observation. Since all the STEM simulations used the same emissions and other settings, these differences come from the differences in the top and lateral boundary conditions. It should be noted that the O_3 overestimations of MOZART-GFDL and RAQMS in this event are not systemic, and later we will see their performances for other scenarios. Figure 6 also shows that the simulated CO with RAQMS BCs is similar to that with MOZART-GFDL BCs, and higher than that with MOZART-NCAR BCs. These differences are consistent with the differences in the corresponding BC concentrations (Figure 3). During the flight segment 1500–1600 UTC, the DC-8 aircraft encountered an elevated concentrated plume which could be either a long-range transported Asian air mass or a biomass burning plume from Alaska and northwestern Canada, and the observed CO concentrations increased along with the altitude. Figure 6 shows that none of the simulations completely captured this feature. However, all of the CO simulations show slight enhancement around 1510 UTC, implying that they captured part of this feature though the enhancement is not as strong and broad as the measurements because of the coarse resolution of the global models or an underestimation of the forest fire plumes.

[18] The O_3 and CO predictions show qualitatively similar distributions but with significant differences in absolute concentrations. For examples, during the flight segment 1300–1900 UTC, the aircraft encountered northwest winds, and the simulation with the MOZART-NCAR top boundary conditions yields much lower O_3 concentrations than those with MOZART-GFDL and RAQMS. In the 10 km layer, the simulation with MOZART-NCAR BCs does not produce O_3 concentrations over 160 ppbv, but the other two simulations yield O_3 concentrations >200 ppbv. In the northwestern corner, the simulation with RAQMS BCs yields O_3 > 250 ppbv. However, all of the STEM simulations show the high-concentration center located around 85°W, 42°N. The simulated CO with MOZART-NCAR BCs is about 20 ppbv lower than the other two simulations in the whole field. RAQMS tends to produce lower CO variability than the two MOZART models for this period. In the air stream from the northwest direction (western side of the trough), the simulations with MOZART-NCAR and MOZAR-GFDL BCs have CO enhancements >20 ppbv compared with their own backgrounds (Figures 5d and 5e), but the

corresponding CO enhancement in the simulation with RAQMS BCs is less than 10 ppbv (Figure 5f). In this case, STEM predicted CO concentrations are strongly influenced by the lateral boundary conditions, and its O_3 predictions rely on both top and lateral boundary conditions. Figure 6 shows that the three simulations have similar low-altitude O_3 concentrations though their high-altitude concentrations differ significantly. On the other hand, the CO concentration differences show smaller variability with altitude.

4. Influence of Temporal and Spatial Variations of Boundary Conditions

[19] As we discussed in the last section, the BC variations from different global models introduce significant variability in the regional predictions. In the absence of dynamic BCs from global models, regional air quality models can use predefined profiles as boundary conditions. Predefined profile BCs are designed to yield reasonable background concentrations for long-lived species, but lack temporal and/or spatial variations. Under some situations for some species, the magnitude of the background concentration is much greater than its spatial and temporal variations, and these variations become less important for certain predictions. This is the reason that predefined profile BCs are useful in regional air quality prediction. Here we perform the sensitivity studies at two scales: 60 km and 12 km, to test the impact of temporal and spatial averaging of the BCs on regional predictions.

[20] Figure 2 shows the framework of these studies. For this sensitivity study, we use the STEM 60 km simulation with MOZART-NCAR BCs as the base case. By performing a temporal average of the lateral and top BCs provided by MOZART-NCAR that cover the entire ICARTT period, we get the temporal mean BCs for the 60 km domain. Through further horizontal averaging of the time-mean lateral boundary condition along its south, north, east and west boundaries, respectively, we get the profile-equivalent lateral BCs: 4 vertical profiles (west, north, east and south) for each species. With these three BCs (original time-varying, time-mean, and profile), we have 3 corresponding simulations in the 60 km domain. The simulation with profile BCs uses the same top BC as that with time-mean BCs. We also performed 3 simulations with a one-way nested 12 km domain covering the northeastern United States, using original, time-fixed and profile BCs derived from the 60 km simulation with the original MOZART-NCAR BCs (Figure 2). Through comparing these simulations, we can test the model's sensitivity to temporal and spatial variation of BCs at different scales. During the ICARTT period, the NASA DC-8 flights covered nearly the entire continental USA, and the NOAA WP-3 flights mainly flew over northeastern USA and surrounding area and captured more of the fine structure of urban plumes. Below, we compare the 60 km simulations to the DC-8 airborne measurements, and the 12 km simulations to the WP-3 observations.

[21] Both the NASA DC-8 and NOAA WP-3 aircrafts had flights on 31 July. The DC-8 aircraft headed to the central North Atlantic and flew back to New Hampshire. Figure 7a shows the 60 km CO simulations compared to the aircraft measurements for the returning segment after 2130 UTC, and the corresponding flight path is shown in Figure 7b. Both the simulations with time-mean and profile BCs tend to overpredict CO by 10–20 ppbv, and the simulation with the original MOZART-NCAR BCs has the best result compared to the measurement. The prediction bias in the profile-BCs simulation is higher than that in time-mean BCs. Figure 7b shows CO horizontal distribution at 3 km predicted with original MOZART-NCAR BCs. Figures 7c and 7d show the difference in the CO predictions at 3 km between the original and averaged BCs. Air masses encountered by this flight mainly come from south and southwest directions (Figure 7). The CO simulation in the 3 km layer with original BCs shows that the inflow CO concentration near the southern inflow boundary region affected this flight is around 70–80 ppbv. The simulated CO with time-mean BCs is 5–20 ppbv higher than that with the original BCs near the southern inflow boundary, and the corresponding difference between the original and profile BCs is even higher. The biggest CO differences appeared near the northern inflow boundary with values up to 70 ppbv in the 3 km layer. In general the spatial difference between the simulations with original BCs and time-mean BCs is similar to that between the original BCs and profile BCs. However, in the northwest part of the domain, the difference between the original and time-mean BCs are positive (Figure 7c) while the difference between the original and profile BCs are negative (Figure 7d).

[22] On the same day, the NOAA WP-3 aircraft performed a nighttime flight over the New England area and sampled the Boston plume. Figure 8 shows the 12 km simulated CO and O_3 concentrations compared to aircraft observation for the segment 2300–2500 UTC. This flight segment is shown in Figure 9, which also shows the nested 12 km domain. During this flight, the aircraft changed altitudes between 3 km to 500 m, but spent most of its time around 1 km. The pollutant concentrations could be affected significantly by near-surface or power plant emissions. Figure 8 shows that the simulations with time-fixed and profile BCs tend to overestimate CO and O_3 for this flight segment, while the simulation with original time-varied BCs yields more reasonable results. The prediction with the original BCs are able to capture the polluted air masses at 2312 UTC, but missed it on the return (2400–2500 UTC) (Figure 7b). It should be noted that these three simulations show similar variations, and the predicted differences are mainly due to their different background concentrations. The simulation with time-fixed BCs yielded about 40 ppbv higher CO and 30 ppbv higher O_3 concentrations than that with original BCs, and the simulation with profile BCs are about 50 and 40 ppbv higher for CO and O_3, respectively. Figure 9 shows the wind field and simulated concentrations in the model's 1 km layer. For this flight segment, the air mass mainly came from south and southwest direction. The 2400–2500 UTC segment encountered a region predicted to be relatively clean with air masses from the ocean in the southeast boundary of this domain, and the simulation with original BCs predicted CO < 80 ppbv and O_3 < 30 ppbv near this boundary. For the same area, the simulation with time-fixed BCs showed CO > 100 ppbv and O_3 > 50 ppbv, and the profile-BCs case had CO > 130 ppbv and O_3 > 65 ppbv (Figure 8). This event analysis clearly shows the model's sensitivity to south inflow boundary conditions. During this period, this domain's west boundary

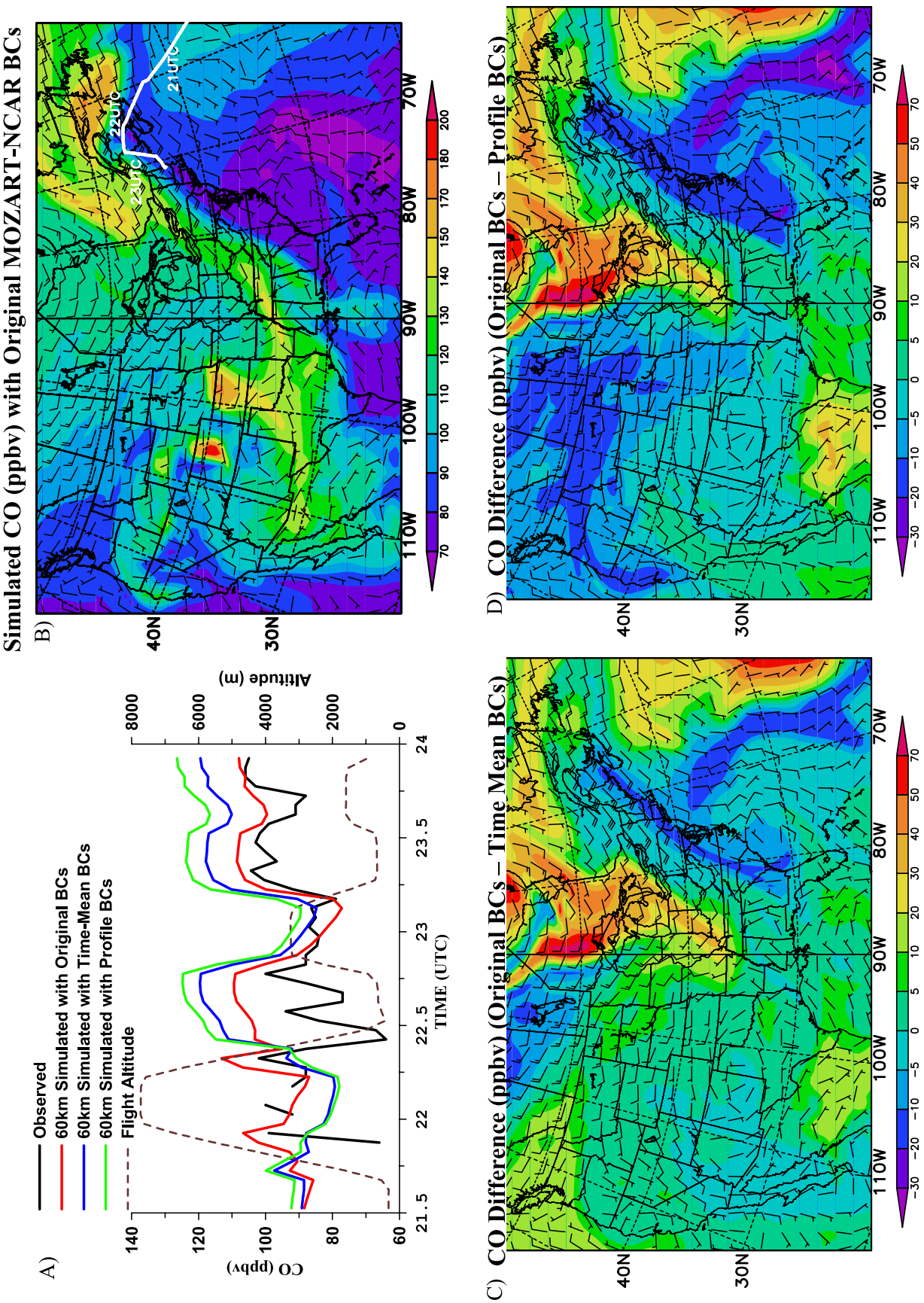

Figure 7. (a) The 60 km simulated CO compared to the DC-8 flight observation on 31 July 2004. (b) Simulated CO with original MOZART-NCAR BCs in the 3 km layer, 0000 UTC, 1 August 2004. (c and d) Corresponding CO differences among the three simulations.

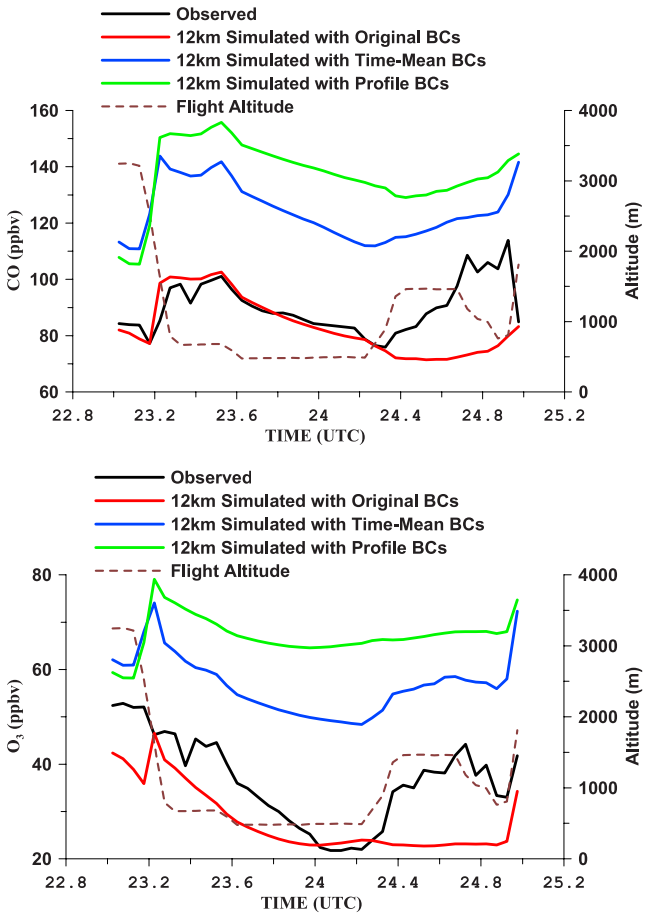

Figure 8. Observed and simulated CO and O_3 concentrations for the WP-3 flight 13 on 31 July to 1 August 2004.

was also an inflow boundary. For the area near the domain's west boundary, the simulation with original BCs predicted up to 100 ppbv higher CO and 60 ppbv higher O_3 concentration than the simulations with time-fixed and profile BCs as the temporal averaging reduced the strong inflow signal of this scenario. During this event, the difference between original BCs and profile BCs is greater than that between original BCs and time-fixed BCs.

[23] These results show that the model's sensitivity to the BCs varies from location to location. The locations near the inflow boundaries have the highest sensitivity to the variation of BCs. This event and the flight on 31 July show that clean areas without strong emission, such as ocean, are more sensitive to the inflow BCs than the polluted areas. In another word, the difference of BCs becomes narrowed faster over polluted areas than that over clean areas.

5. Overall Evaluation

[24] Through the scenario analysis discussed above, we showed the regional model's dependence on lateral and top boundary conditions. However, these analyses are based on specific events, and did not give an overall picture. In this section we analyze the effect of BCs using statistical and other methods.

5.1. Statistical Results Due to Different Global BCs Compared to Aircraft Measurements

[25] Table 2 shows the correlations between the DC-8 observations and the simulations with boundary conditions from the global models for three vertical layers. The statistical results include mean values that represent the concentration magnitudes, correlation coefficient R that reflects the synchronism of the simulations for the temporal and spatial variations, and the regression slope that reflects the amplitude of the simulated variations compared to observation. The DC-8 flight paths covered large portions of the USA during the ICARTT period, with altitude ranging from 200 m to 12 km. Figure 1 shows the NASA DC-8 and NOAA WP-3 flight paths during this period. The three simulations have a very similar performance for O_3 predictions below 3 km, implying that the boundary conditions have weaker impact on low-altitude O_3 predictions in this domain. The O_3 simulations at higher altitudes (>3 km) mainly reflect the difference of BCs from the three global models, and they are also very similar in correlation coefficient R. The differences among 60 km STEM regional predictions mainly reflect the different BCs from the corresponding global models. The STEM CO simulation with RAQMS BCs yielded the highest correlation coefficient R, which is consistent with the global model performance.

[26] A similar comparison for the NOAA WP-3 flights is shown in Table 3. The WP-3 aircraft mainly flew over the northeastern USA with altitudes ranging from 200 m to 7 km, including many research flights studying urban plumes. For the O_3 prediction below 3 km, the difference among these simulations is relatively insignificant compared to that for DC-8 flights. The influence of boundary conditions on CO prediction is relatively stronger than that on O_3 in all layers. In general, the differences among these three simulations for WP-3 flights are smaller than those for DC-8 flights as the DC-8 flew over broader regions and at higher altitudes, and had more flight paths near the domain's lateral and top boundaries. For long-lived high-concentration species, like CO, the influence due to different boundary conditions can be shown throughout the domain. During the ICARTT period, the most significant CO inflow was the forest fire plumes from Alaska and Canada, which entered the STEM 60 km domain from its north lateral boundary. The most significant O_3 inflow occurred near the domain top from the stratosphere, which affected DC-8 flights more than WP-3 flights. For most short-lived emitted species, the influence of BCs is relatively weak as the strong emissions within the domain show greater impact.

[27] Figure 10 shows the O_3 and CO mean vertical profiles and standard deviations for these DC-8 and WP-3 flights. The predicted CO profiles show that the model sensitivity to BCs is throughout the tropospheric. Even near the surface, the mean CO values differ by about 40 ppbv. Both aircraft measurements show that the biggest CO standard deviation appears in altitudes from 2.5 to 4 km, which reflect the turbulent lofting within the planetary boundary layer (PBL), convection and forest fire plumes. However, none of the simulations captured the magnitude of the observed variation. The simulation with MOZART-GFDL BCs tended to overpredict the mean CO below 6 km for the WP-3 flights, and below 8 km for DC-8 flights,

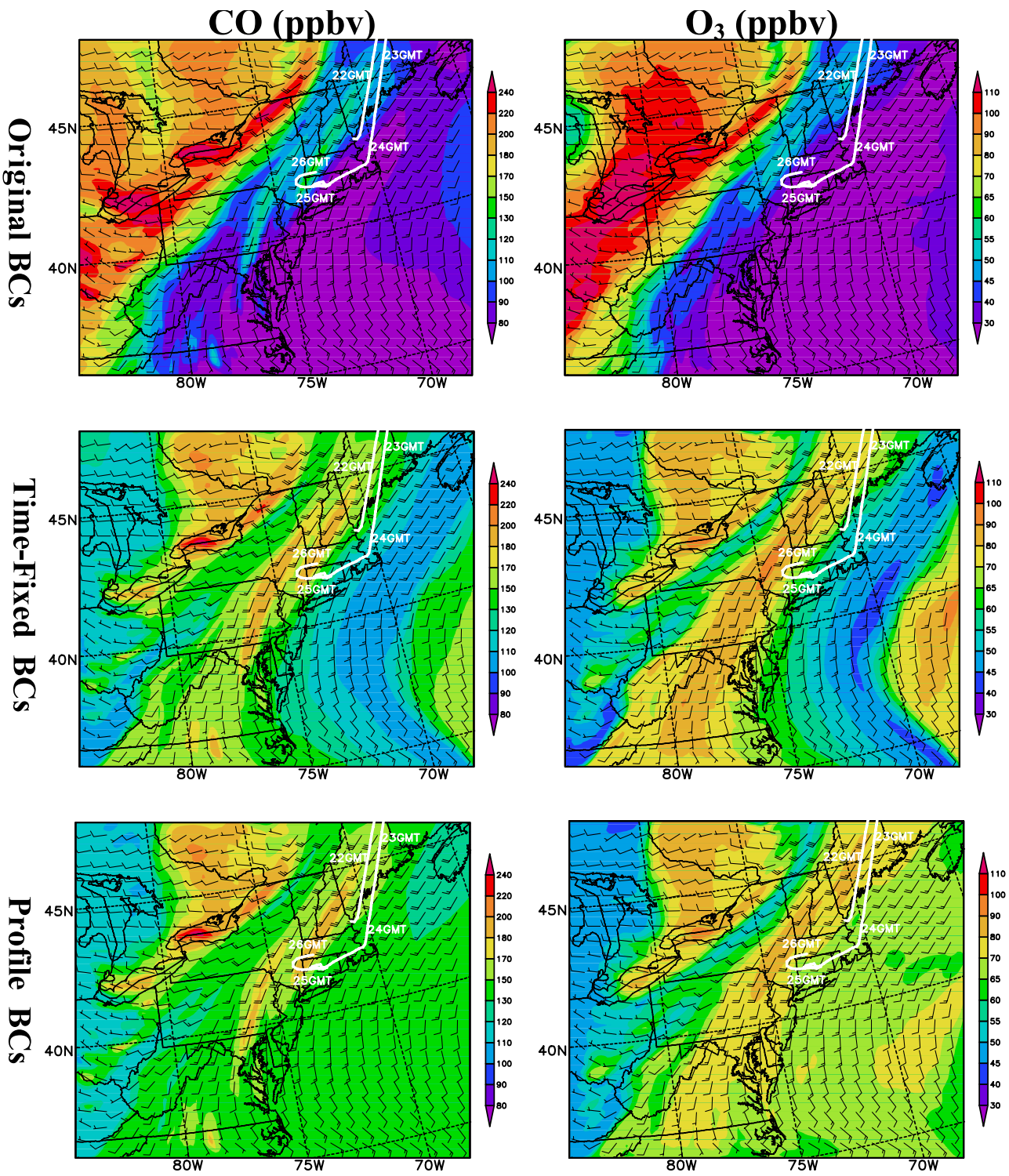

Figure 9. The 12 km simulated (left) CO and (right) O_3 concentrations in the 1 km layer, at 0000 UTC, 1 August 2004, driven by three different boundary conditions. The WP-3 flight path is shown in each plot.

while the simulation driven by MOZART-NCAR BCs underestimated CO above 4 km (Figures 10a and 10c). O_3 predictions below 3 km are insensitive to the global BCs. Above 8 km, the O_3 differences among the STEM simulations are mainly determined by the global top BCs, and the O_3 mean values have RAQMS > MOZART-GFDL > MOZART-NCAR (Figure 10b), which is consistent with the general trends of global models shown in Figure 2. Figure 10b also shows that the simulation with MOZART-NCAR BCs underestimated the O_3 deviation in this top

Table 2. Statistic Result of 60 km Simulations With the Three Boundary Conditions Compared With the Observations in NASA DC-8 Flights 3–20[a]

		60 km Simulated With MOZART-NCAR BCs			60 km Simulated With MOZART-GFDL BCs			60 km Simulated With RAQMS BCs		
Species	Observed Mean	Simulated Mean	Slope	R	Simulated Mean	Slope	R	Simulated Mean	Slope	R
O_3, ppbv (<1 km)	47.0	52.7	0.84	0.71	52.4	0.91	0.71	53.2	0.88	0.72
O_3, ppbv (1–3 km)	54.0	56.3	0.77	0.54	55.9	0.82	0.53	57.5	0.80	0.56
O_3, ppbv (>3 km)	77.7	65.0	0.21	0.51	67.8	0.40	0.54	86.4	0.70	0.51
CO, ppbv (<1 km)	136.0	137.2	0.94	0.65	179.6	1.66	0.62	150.1	1.27	0.79
CO, ppbv (1–3 km)	122.4	131.7	1.14	0.69	172.3	2.16	0.65	142.2	1.43	0.80
CO, ppbv (>3 km)	102.2	89.3	0.74	0.38	112.0	1.44	0.43	96.0	0.53	0.41

[a]The correlation slope and coefficient (R) are presented in model (y) versus observation (x).

altitude, and the other simulations resulted in larger variations. All observations and models found that the minimum O_3 standard deviation was in the altitude 3–5 km. The small O_3 deviation above 6 km for WP-3 flights (Figure 10d) is mainly due to its relatively few data points.

[28] The differences among these 60 km STEM regional simulations mainly reflect the differences in these three global models. We also compare the regional model predictions to global model predictions, in order to assess the impact of the regional model on predicting tropospheric O_3 and CO distributions. Equivalent predictions were compared; for example, the RAQMS prediction is compared to the STEM simulation with the RAQMS BCs. Our statistical comparison indicates that the STEM predictions yielded higher R values and slope closer to 1 than the corresponding global models at the altitudes below 3 km (not shown). Figure 11 shows the similar results to Figure 10, but for the performances of the three global models themselves during ICARTT flights. These global models cover the all the DC-8 and WP-3 flight paths, while the STEM 60 km domain missed some DC-8 flight segments. One can see from Figures 10 and 11 that the STEM simulations consistently reflect the CO and O_3 concentration trend brought from the global models, especially in the high altitudes. However, the difference between the regional and global models is also evident. For instance, the STEM simulations for DC-8 flight tend to yield lower CO concentration above 8 km than the corresponding global models, reflecting the different CO loss rates in regional and global models. In low altitudes, boundary conditions from global models have little influence on O_3 prediction, reflected by the nearly overlapped STEM O_3 profiles below 2 km (Figures 10b and 10d), though the O_3 predictions of global models are different (Figures 11b and 11d). The BC influences on CO are more complex. One of the reasons is that CO has longer lifetime than O_3 and the inflow CO from lateral boundaries could have evident impact throughout the whole STEM regional domain. The MOZART-GFDL and the STEM simulation driven by its BC show systematically higher CO concentrations than the other models and corresponding STEM simulations (Figures 10a, 10c, 11a, and 11c). The CO concentration is also affected by other species, such as hydrocarbons, since CO is an intermediate product of most hydrocarbon oxidization, and hydrocarbons compete with CO for OH, which result in lower CO consumption. RAQMS and MOZART-NCAR has different hydrocarbon concentrations and speciation. When we use these hydrocarbon concentrations to feed the SAPRC99 mechanism used in the STEM model, the STEM simulations show different impacts on CO from the global models.

5.2. Statistical Results of Model Sensitivity to Temporal and Spatial Variations of Boundary Conditions

[29] We also analyzed the difference among the simulations with original time-varied BCs, time-mean BCs, and profile BCs in the 60 km and 12 km domains. Table 4 is similar to Table 2 but for the 60 km simulations with original MOZART-NCAR, time-mean and profile boundary conditions. The 60 km simulations with the original MOZART-NCAR BCs has a better correlation slope and coefficient (R) than those with averaged BCs for O_3. It is reasonable because temporal and spatial averaging remove O_3 variation information from the top and lateral boundaries. In low altitudes (<3 km), the simulations with averaged BCs have higher mean bias for O_3. However, the time-varied BCs do not show advantage on predicting the mean CO values. Their difference on CO prediction is

Table 3. Statistic Result of 60 km Simulations With the Three Boundary Conditions Compared With the Observations in All NOAA WP-3 Research Flights[a]

		60 km Simulated With MOZART-NCAR BCs			60 km Simulated With MOZART-GFDL BCs			60 km Simulated With RAQMS BCs		
Species	Observed Mean	Simulated Mean	Slope	R	Simulated Mean	Slope	R	Simulated Mean	Slope	R
O_3, ppbv (<1 km)	56.2	54.6	0.62	0.62	55.0	0.66	0.63	54.9	0.61	0.62
O_3, ppbv (1–3 km)	60.6	63.8	0.72	0.57	63.8	0.75	0.55	65.1	0.71	0.58
O_3, ppbv (>3 km)	65.1	60.3	0.44	0.42	58.0	0.42	0.35	66.6	0.49	0.47
CO, ppbv (<1 km)	158.3	161.7	1.01	0.45	207.6	1.94	0.40	170.2	1.16	0.57
CO, ppbv (1–3 km)	140.6	148.5	0.78	0.60	191.5	1.31	0.60	163.4	1.25	0.72
CO, ppbv (>3 km)	108.6	104.4	0.42	0.46	135.0	0.92	0.49	114. 5	0.86	0.67

[a]The correlation slope and coefficient (R) are presented in model (y) versus observation (x).

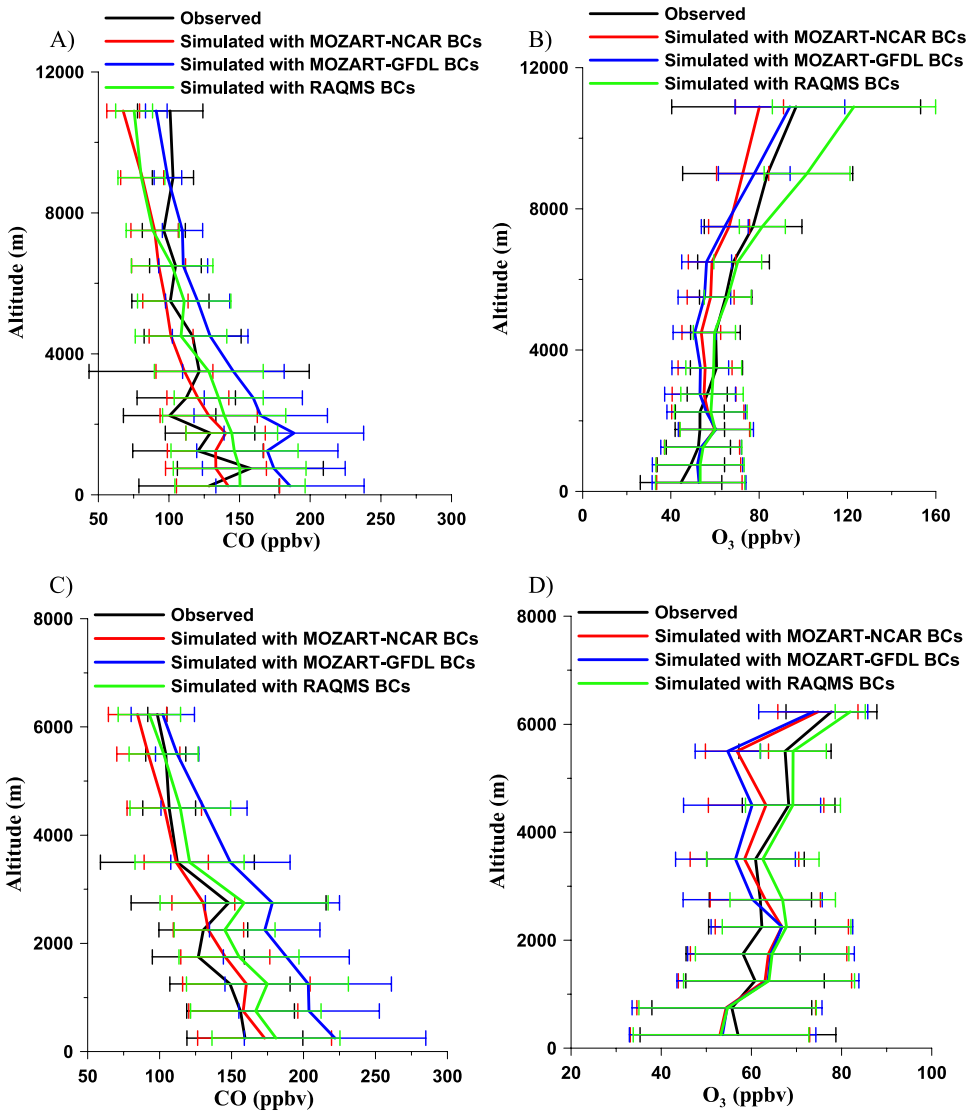

Figure 10. Observed and 60-km-simulated CO and O_3 mean profiles and standard deviations for (a and b) all DC-8 flights and (c and d) WP-3 flights.

smaller than that for O_3, because original inflow BCs for the CO do not have variations as strong as for O_3 whose variations are mainly from stratospheric O_3, except for special events, such as forest fire plumes. In general, the difference among these cases is relatively small since most DC-8 flights are far away from the inflow boundary, and the variation of BCs was not very strong.

[30] The corresponding results for 12 km simulations compared to NOAA WP-3 observation are shown in Table 5. It should be noted that the 12 km domain covered most, but not all of the WP-3 flights. We just chose the flight segments covered by the 12 km domain for this comparison. These statistical results do show the advantage of higher resolution as the 12 km simulation (Table 5) yielded better correlation coefficients and slopes than the 60 km simulation (Table 3) for CO and O_3 at low altitudes, as the higher resolution can better capture the variations of surface emissions for the WP-3 flight segments over northeastern USA. The difference among the different BCs is more significant in the 12 km simulation than in the 60 km simulation. The simulation with original BCs is better than the simulations with time-mean and profile BCs for most species. For the 12 km domain, the major inflow forcing comes from its upwind areas, including U.S. Midwest and California, with high pollutant emissions. For instance, Chicago is one of major regional contributors to inflow pollutants in the 12 km domain. The weather-driven airflow can bring the strong and distinct upwind Chicago signals to this domain. After temporal and spatial averaging, this signal becomes relatively uniform. In contrast, the 60 km domain's inflow boundary is located over relatively clean areas, like the eastern Pacific and Canada, where the natural pollutant signals are relatively uniform after long-range transport and dynamical diffusion (except for some special events). So the 60 km domain is not as sensitive to the removal of temporal and spatial variations on BCs as the nested 12 km domain. In the 12 km domain, the time-varied BCs also yield better results for secondary species, such as PAN and O_3.

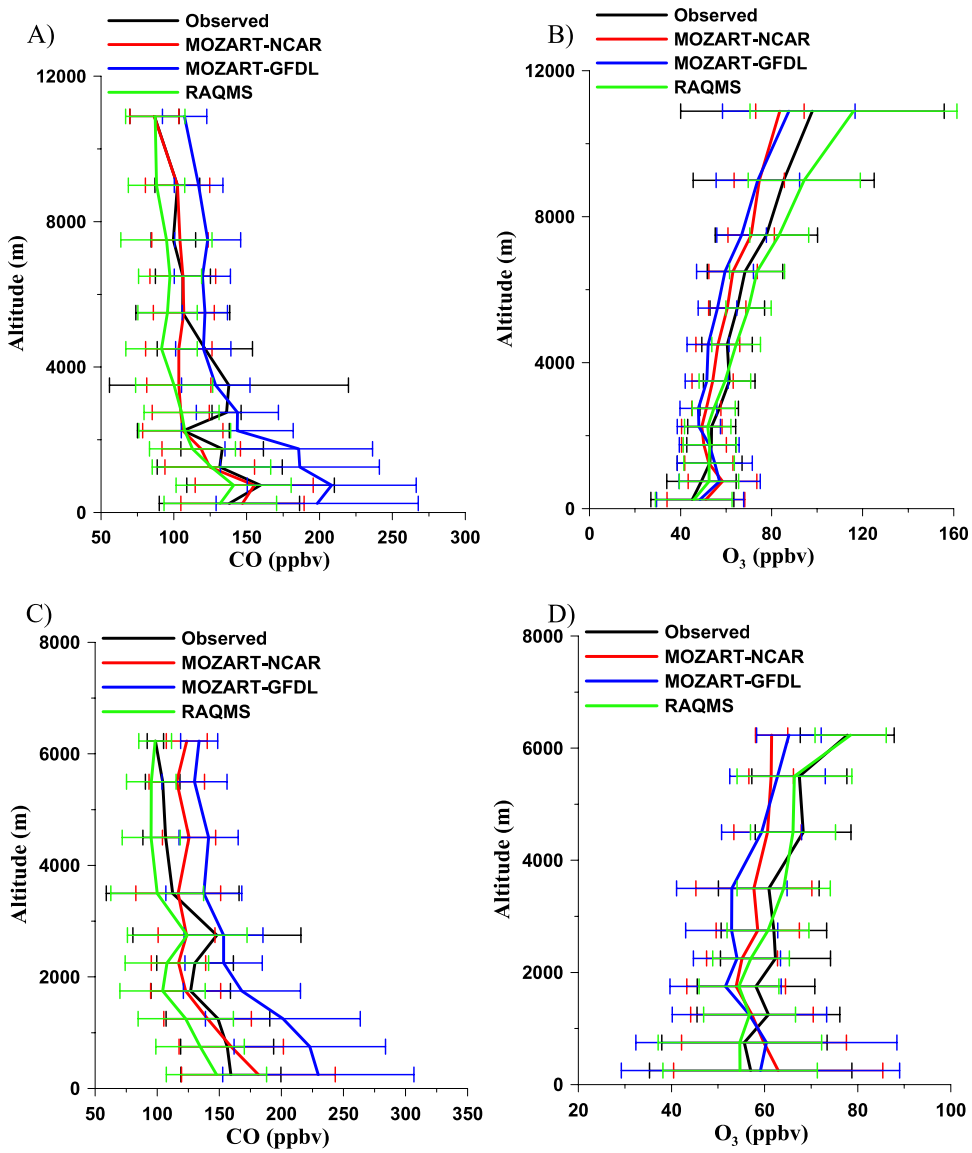

Figure 11. Observed and global model simulated O_3 mean profiles and standard deviations for (a and b) all DC-8 flights and (c and d) WP-3 flights.

[31] To further investigate the model's sensitivity to temporal and spatial variations of boundary conditions and its dependence on location and scale, we compare the predicted CO vertical profiles for the model grid points 5 grid cells from the west, east, south and north boundaries of the 60 km simulations in Figure 12, which shows mean values and standard deviations of the predicted/observed concentrations. The west boundary is mainly located along the U.S. west coast, where California emissions are a strong contributor to CO. So, all the three simulations with original, time-mean and profile BCs show similar strong CO deviations at low altitudes, and this deviation decreases with altitude near the west boundary. As expect, the standard deviations decrease for the simulations with time-mean and profile BCs since variations are reduced because of averaging. The biggest difference among these simulations is the CO standard deviation above 9 km near the west inflow boundary, where the simulation with original BCs shows much greater variation than the others, though they have similar mean concentration. During the summertime, Asian air mass inflow still exists, but not as strong as that during springtime. The CO standard deviation in the simulation with the original BCs is about 5 ppbv at altitudes above 9 km. The other two simulations remove the temporal and both temporal and spatial variations from the lateral boundary, and so their variations become much weaker. In the 60 km domain, the simulated mean values along the prevailing inflow lateral boundaries are little affected by the averaging process.

[32] The east boundary is the prevailing outflow boundary of this 60 km domain, but Figure 12b still shows that the simulation with original BCs yielded greater standard deviations than the simulations with averaged BCs, especially in the high altitudes. Near the south boundary, the simulations have the minimum differences in their standard deviations, even at high altitudes. The most significant difference in the

Table 4. Statistic Results of 60 km Simulations With the Original MOZART-NCAR, Time-Mean and Profile Boundary Conditions Compared With the Observations in NASA DC-8 Flights 3–20[a]

		60 km Simulated With MOZART-NCAR BCs			60 km Simulated With Time-Mean BCs			60 km Simulated With Profile BCs		
Species	Observed Mean	Simulated Mean	Slope	R	Simulated Mean	Slope	R	Simulated Mean	Slope	R
O_3, ppbv (<1 km)	47.0	52.7	0.84	0.71	59.2	0.84	0.68	59.3	0.84	0.68
O_3, ppbv (1–3 km)	54.0	56.3	0.77	0.54	60.5	0.63	0.54	60.5	0.62	0.54
O_3, ppbv (>3 km)	77.7	65.0	0.21	0.51	65.3	0.18	0.49	64.5	0.17	0.50
CO, ppbv (<1 km)	136.0	137.2	0.94	0.65	138.8	0.83	0.65	138.4	0.80	0.64
CO, ppbv (1–3 km)	122.4	131.7	1.14	0.69	132.8	1.01	0.67	132.0	0.96	0.66
CO, ppbv (>3 km)	102.2	89.3	0.74	0.38	90.0	0.58	0.37	89.5	0.49	0.38

[a]The correlation slope and coefficient (R) are presented in model (y) versus observation (x).

CO standard deviations exists along the north boundary. For the north boundary, these simulations make the biggest difference on the CO standard deviation. The original BCs contain strong and highly time-varied CO inflows, reflecting the effects of forest fires and Asian plumes. The simulation with the original MOZART-NCAR BCs shows strong CO variation in the altitudes from 6 km to 9 km. Temporal and spatial averagings reduce the impact of events. Furthermore the use of averaged BC produced mean concentration biases (Figure 12d).

[33] Figure 13 shows the corresponding comparison for the 12 km domain covering the northeastern USA. In this domain, the prevailing inflow boundaries are also located in the west and north. The CO variability in the 12 km domain is higher than that in the 60 km domain, reflecting the difference in regional resolution. The only exception is for the south boundary (Figure 13c), which had weak variations, and all three simulations yielded similar mean CO profiles near the south boundary. Near all the other boundaries, the simulation with original BCs produces larger CO variations than the two simulations with averaged BCs, and even has a different mean CO profile. Figure 13a shows that the three simulations show similar CO standard deviations below 2 km, because of their same emissions, but the mean CO profiles differ significantly, while the simulation with the original BCs yielded the higher CO mean concentration. This simulation also has the higher CO variations in the east and north boundaries at low altitudes. Near all the four boundaries, the simulation with original BCs has higher CO variation in high altitudes than the other two, which is similar to the case in the 60 km domain. The CO variation difference among these simulations in low altitudes reflects that the simulations with averaged BCs fail to represent the CO emission and transport from polluted upwind areas, which could immediately adjoin to the model domain.

5.3. Contribution of Lateral Boundary Conditions Represented by Influence Functions

[34] The above discussion shows that the sensitivity at a given location to boundary conditions depends on the domain characteristics, such as wind field, emissions and strength of boundary flux. To more quantitatively describe these characteristics, we introduce an influence function as

$$C_i(x,y,z) = \sum_{n=0}^{N-1} \lambda_i(x,y,z,t) \quad (1)$$

where i is the chemical species index, N is the total number of time steps, and $\lambda_i(x,y,z,t)$ is the adjoint variable calculated from STEM adjoint model [*Sandu et al.*, 2005; *Chai et al.*, 2006]. After choosing a target species and target region at a certain time, $\lambda_i(x,y,z,t)$ (unitless variable: concentration/concentration) is the sensitivity function of the target with respect to $C_i(x,y,z,t)$. Thus the time-integrated sensitivity, i.e., the influence function $C_i(x,y,z)$, can provide information on how the model predictions are affected by the boundary conditions. Figure 14 shows the 5-day integrated (19–24 July) $\lambda_{co}(x,y,z)$ (CO as target species) distribution with the MOZART-NCAR boundary condition in our 60 km domain for the target subdomain ($33 \times 21 \times 7$ grid points) shown in Figure 14a. Here the influence function is defined as the mean influence of each grid cell in the lateral boundary on the grid cells in the target subdomain. The target region has a vertical extent from 1 to 4 km above ground. From 19 to 24 July, the prevailing wind influx to the target region in the 3 km level

Table 5. Statistic Result of 12 km Simulations With the Original, Time-Mean and Profile Boundary Conditions Compared With the Observations in All NOAA WP-3 Research Flights Covered by the 12 km Domain[a]

		12 km Simulated With Original BCs			12 km Simulated With Time-Mean BCs			12 km Simulated With Profile BCs		
Species	Observed Mean	Simulated Mean	Slope	R	Simulated Mean	Slope	R	Simulated Mean	Slope	R
O_3, ppbv (<1 km)	56.2	60.1	0.77	0.72	64.7	0.50	0.69	65.5	0.48	0.67
O_3, ppbv (1–3 km)	60.6	67.9	0.75	0.59	68.2	0.35	0.42	68.0	0.34	0.42
O_3, ppbv (>3 km)	65.1	62.4	0.36	0.38	55.1	0.07	0.16	54.8	0.10	0.24
CO, ppbv (<1 km)	158.3	165.7	1.06	0.54	165.1	0.58	0.47	165.6	0.55	0.44
CO, ppbv (1–3 km)	140.6	152.9	0.84	0.60	150.5	0.49	0.43	149.7	0.50	0.44
CO, ppbv (>3 km)	108.6	104.4	0.42	0.45	102.1	0.13	0.32	101.3	0.15	0.41

[a]The correlation slope and coefficient (R) are presented in model (y) versus observation (x).

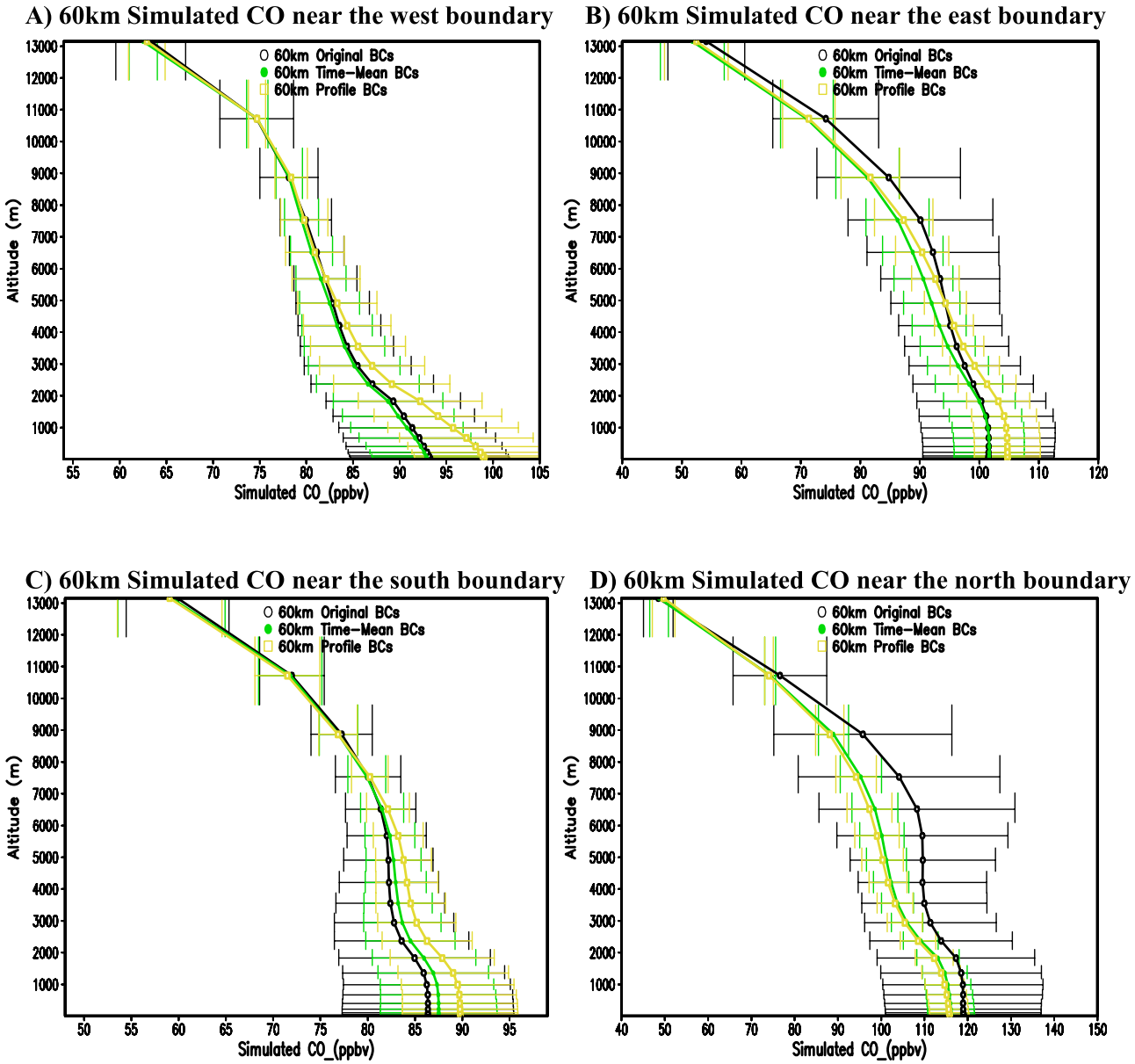

Figure 12. Simulated CO mean concentrations and standard deviation with original MOZART-NCAR, time-mean and profile boundary conditions over the grid lines that are 5 grid cells from (a) west, (b) east, (c) south and (d) north boundaries in the 60 km domain.

(Figure 14a) came from northwest and southwest, and the southwest wind was relatively weaker. Figure 14a illustrates the vertically integrated influence of the whole-field CO on CO concentrations in the target subdomain. The emission sources from Texas have a strong influence on the target area during this period. In addition to this emission influence, the north boundary condition is the major influencing factor, which extends an area of the influence from northwest boundary to the target area. Figure 14b shows the vertical extent of the CO-on-CO influence function along the cross section of the north boundary of the 60 km domain over continental USA, and we can see that the high influence came from altitudes 1–3 km, and these high CO levels were due to forest fires in Canada and Alaska. Figure 14c shows mean profile of this influence function and its spatial standard deviation along the 4 lateral boundaries during this 5-day period. The north boundary shows the biggest influence on this domain with peak value at ~2 km, while south boundary's influence existed mainly below 3 km. The boundary showed influence above 3 km due to the CO pollutant from Asia or recirculated pollutants from U.S west coast. The east boundary has relatively weak influence as it is the prevailing outflow boundary throughout this period. The O_3-on-O_3 influence function is similar to CO-on-CO but its peak values appear at higher altitudes: 3 km (Figure 14d), which reflect upper layer ozone contributions. Figure 14e shows the chemical contribution of CO to O_3 in this influence function. In this case, CO mainly

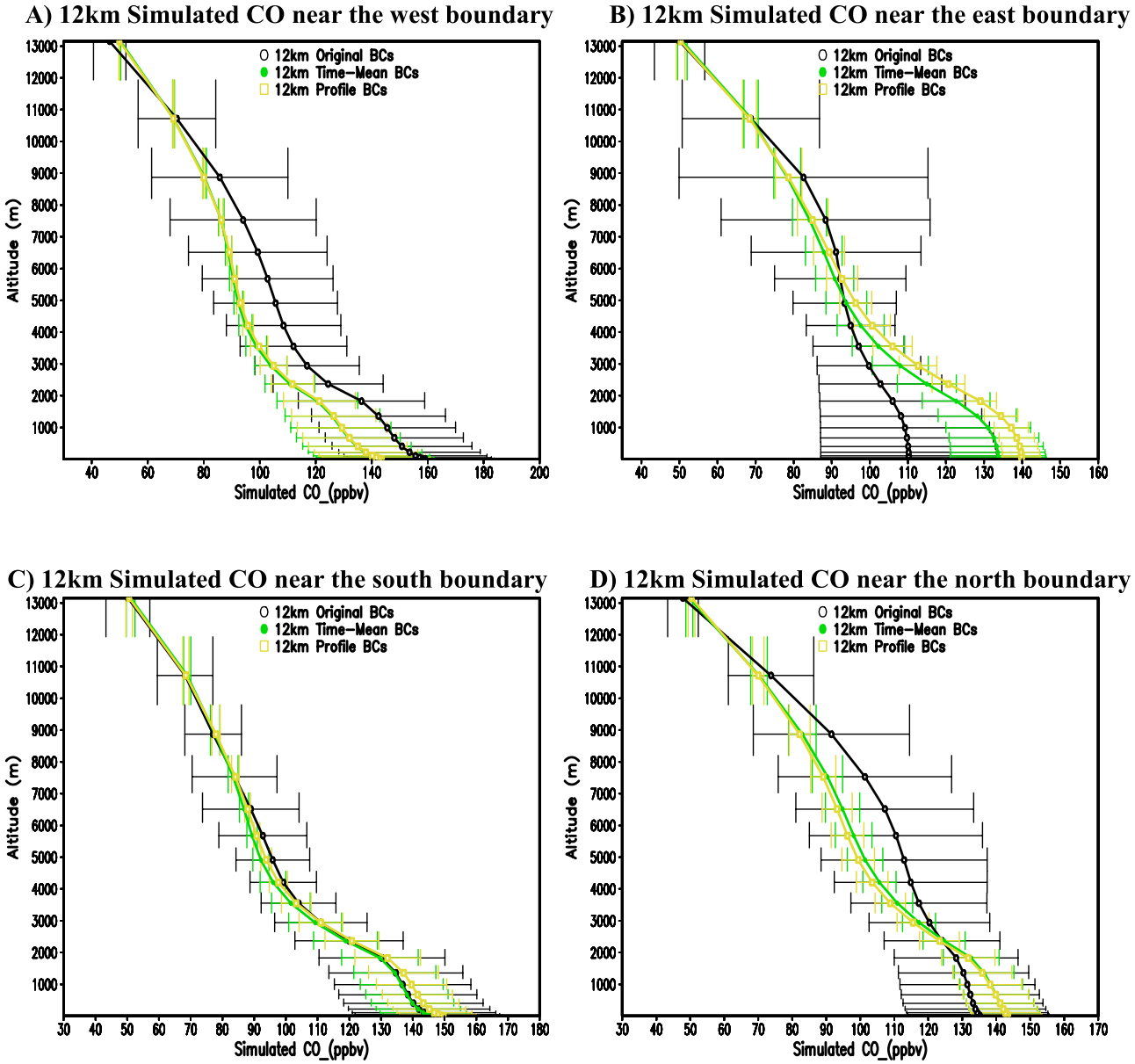

Figure 13. Simulated CO mean concentrations and standard deviation with original time-varied, time-mean and profile boundary conditions over the grid lines that are five grid cells from (a) west, (b) east, (c) south and (d) north boundaries in the 12 km domain.

contributes to O_3 photochemical production by pumping NO to NO_2:

$$CO + OH + O_2 \rightarrow CO_2 + HO_2$$

$$HO_2 + NO \rightarrow NO_2 + OH$$

$$NO_2 \xrightarrow{\lambda} NO + O^3P$$

$$O^3P + O_2 \rightarrow O_3$$

[35] The west boundary inflow of CO shows the highest O_3 production efficiency, and the north boundary has the lowest one. This chemical conversion mainly depends on which kinds of air mass mix with the boundary inflow CO. Near west and south inflow boundaries, there are abundant NO_x emissions that benefit CO contribution to O_3, while the region near the north boundary (north Dakota et al.) are relatively clean.

6. Conclusion

[36] In this study, the sensitivity of regional air quality predictions to the treatment of boundary conditions (BCs) was studied. We performed simulations with BCs from three different global models. We also performed simulations to test the impact of temporal and spatial averaging of the BCs

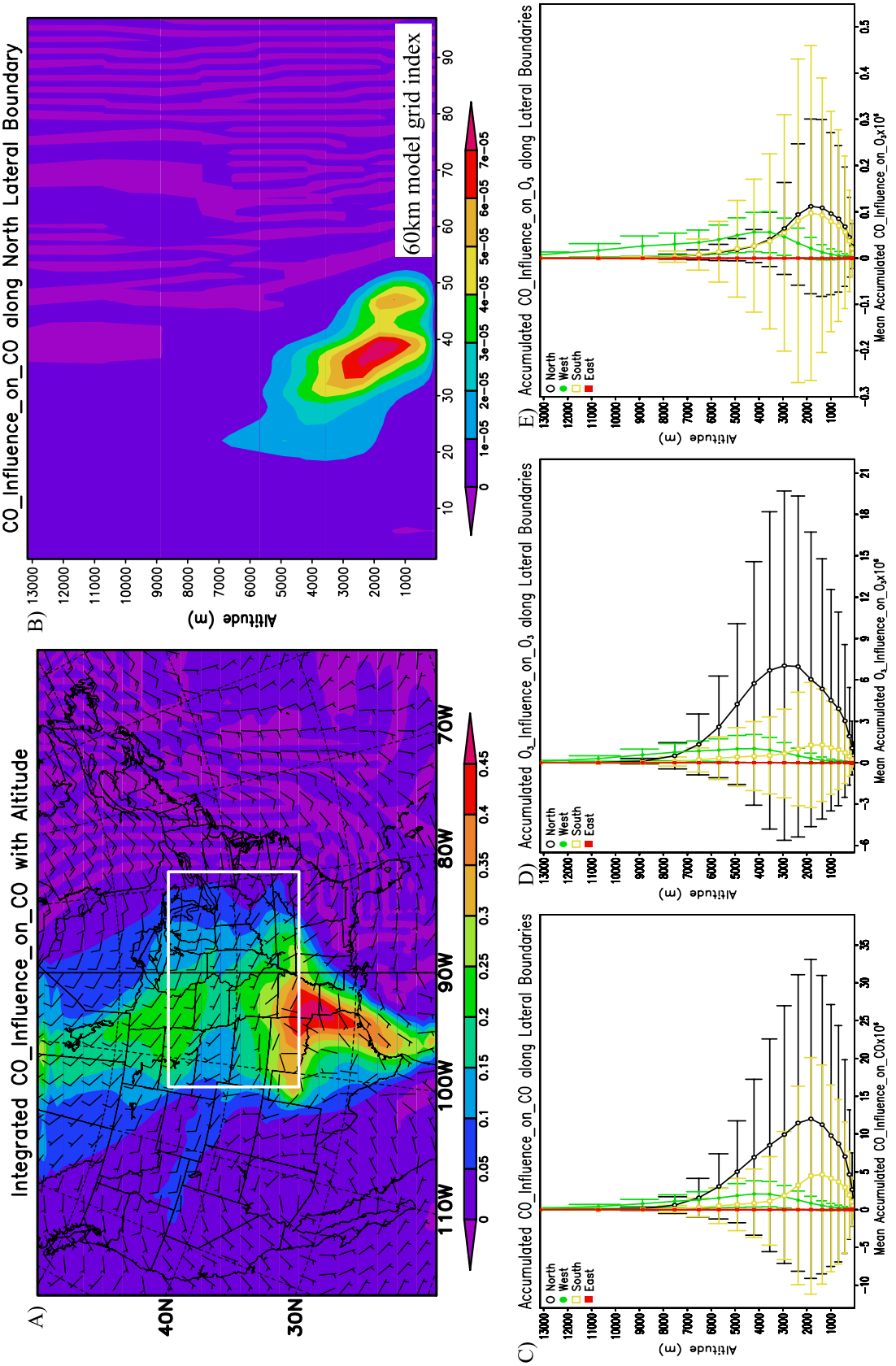

Figure 14. Influence function distributions: (a) integrated with altitude and time-mean wind in 3 km, (b) north boundary and (c–e) mean and standard deviations along the four lateral boundaries. The influence functions are integrated from 19 to 24 July for the target grid box with vertical elevation 1–4 km shown in Figure 14a.

on the air quality predictions. These results have important implication for air quality modeling, as the treatment of BCs is recognizes as a large source of uncertainty. In the past air quality predictions have had to rely on the use of climatological, and often fixed, BCs. As global model predictions have become available, regional air quality models are beginning to use BCs from the global models. Since during the ICARTT experiments several global model predictions were performed, this presented an excellent opportunity to test the impact of the global models BCs on the regional predictions.

[37] Our model results demonstrate that the use of global BCs results in improved model predictions. The most important advantage of using global model BCs is that these BCs can bring time-varied external signals to the regional domain, and reflect certain event information, such as biomass burning, stratospheric intrusion, and Asian air mass inflow. These variabilities are shown to be important in achieving a predicted variability I the regional model that is similar to that in the observed distributions.

[38] The results from using three different global model BCs point out that the global models themselves are a major source of uncertainty in the regional-scale predictions. The differences between the global model BCs reflect differences in their chemical schemes, configurations (including grid size), meteorology and emissions, and treatments of stratospheric/tropospheric exchange. Comparison of the regional model predictions with ICARTT aircraft observations shows that the mission wide mean ozone distributions below $\sim$3 km are insensitive to the global BCs, while the values in the mid to upper troposphere are dominated by the global model BCs. This reflect the fact that ozone processes in the lower troposphere are dominated by local processes (i.e., emissions, chemical production/destruction). For long-lived species such as CO, the impact of the BCs is felt at high altitudes and at the surface, where the near surface mean CO values differ between the different BCs by over 40 ppb.

[39] Results from the sensitivity of the regional predictions to temporal and spatial averaging of the BCs show that the effects can be important. For example results from the case studies for the ozone and CO in the eastern United States, show that the use of average BCs results in a substantial increase in near surface concentrations. In addition the averaged profiles significantly reduces the regional model predicted variability. The result showed that these effects are larger for the 12 km domain than for the 60 km domain. In addition the results showed that both temporal and spatial variability are important. However, the mission-wide mean values were rather insensitive to the BC averaging (but the slopes and correlations were effected).

[40] These results suggest that the use of global model BCs can improve regional air quality predictions. These results also point out that further improvement in regional model predictions will require efforts to reduce the uncertainty in the global model BCs. One approach to better prediction would be to use an ensemble of predictions based on different global boundary conditions. Another approach would be to develop data assimilation methods to better constrain the global model BCs. These approaches are areas of follow-on study. Finally it should be noted that this study covers only the ICARTT period (about 1.5 months) and focuses on certain events. Further study over longer time periods are needed better answer assess the role of the BC treatment.

[41] **Acknowledgments.** This work was supported in part by grants from the NASA Tropospheric Chemistry Program, the NOAA Global Change Program, and the NSF Atmospheric Chemistry/ITR programs.

References

Carter, W. (2000), Documentation of the SAPRC-99 chemical mechanism for voc reactivity assessment, final report to California Air Resources Board, contract 92-329, Univ. of Calif., Riverside, 8 May.

Chai, T., G. R. Carmichael, A. Sandu, Y. Tang, and D. N. Daescu (2006), Chemical data assimilation of transport and chemical evolution over the Pacific (TRACE-P) aircraft measurements, *J. Geophys. Res.*, *111*, D02301, doi:10.1029/2005JD005883.

Chen, K. S., Y. T. Ho, C. H. Lai, and Y.-M. Chou (2003), Photochemical modeling and analysis of meteorological parameters during ozone episodes in Kaohsiung, Taiwan, *Atmos. Environ.*, *37*, 1811–1823.

Duncan, B. N., and I. Bey (2004), A modeling study of the export pathways of pollution from Europe: Seasonal and interannual variations (1987–1997), *J. Geophys. Res.*, *109*, D08301, doi:10.1029/2003JD004079.

Emmons, L. K., G. G. Pfister, D. P. Edwards, J. C. Gille, G. Sachse, D. Blake, S. Wofsy, C. Gerbig, D. Matross, and P. Nédélec (2007), Measurements of Pollution in the Troposphere (MOPITT) validation exercises during summer 2004 field campaigns over North America, *J. Geophys. Res.*, *112*, D12S02, doi:10.1029/2006JD007833.

Frost, G. J., et al. (2006), Effects of changing power plant NO_x emissions on ozone in the eastern United States: Proof of concept, *J. Geophys. Res.*, *111*, D12306, doi:10.1029/2005JD006354.

Geron, C. D., A. B. Guenther, and T. E. Pierce (1994), An improved model for estimating emissions of volatile organic compounds from forests in the eastern United States, *J. Geophys. Res.*, *99*(D6), 12,773–12,791.

Gong, S. L. (2003), A parameterization of sea-salt aerosol source function for sub- and super-micron particles, *Global Biogeochem. Cycles*, *17*(4), 1097, doi:10.1029/2003GB002079.

Granier, C., et al. (2004), Present and future surface emissions of atmospheric compounds, *Rep. EVK 2199900011,* Eur. Comm., Brussels.

Grell, G. A., J. Dudhia, and D. R. Stauffer (1994), A description of the fifth-generation Penn State/NCAR mesoscale model (MM5), *NCAR Technical Note, NCAR/TN-398+STR,* 117 pp., Natl. Cent. for Atmos. Res., Boulder, Colo.

Hong, S.-Y., and H.-L. Pan (1996), Nonlocal boundary layer vertical diffusion in a medium-range forecast model, *Mon. Weather Rev.*, *124*, 2322–2339.

Horowitz, L. W., et al. (2003), A global simulation of tropospheric ozone and related tracers: Description and evaluation of MOZART, version 2, *J. Geophys. Res.*, *108*(D24), 4784, doi:10.1029/2002JD002853.

Horowitz, L. W., et al. (2007), Observational constraints on the chemistry of isoprene nitrates over the eastern United States, *J. Geophys. Res.*, doi:10.1029/2006JD007747, in press.

Kim, Y. P., J. H. Seinfeld, and P. Saxena (1993a), Atmospheric gas-aerosol equilibrium I: Thermodynamic model, *Aerosol Sci. Technol.*, *19*, 151–181.

Kim, Y. P., J. H. Seinfeld, and P. Saxena (1993b), Atmospheric gas-aerosol equilibrium II: Analysis of common approximations and activity coefficient calculation methods, *Aerosol Sci. Technol.*, *19*, 182–198.

Kim, Y. P., and J. H. Seinfeld (1995), Atmospheric gas-aerosol equilibrium III: Thermodynamics of crustal elements Ca^{2+}, K^{+}, Mg^{2+}, *Aerosol Sci. Technol.*, *22*, 93–110.

McLinden, C. A., S. C. Olsen, B. Hannegan, O. Wild, and M. J. Prather (2000), Stratospheric ozone in 3-D models: A simple chemistry and the cross-tropopause flux, *J. Geophys. Res.*, *105*(D11), 14,653–14,665.

Olivier, J. G. J., and J. J. M. Berdowski (2001), Global emissions sources and sinks, in *The Climate System*, edited by Berdowski, J., R. Guicherit, and B. J. Heij, pp. 33–78, Balkema, A. A. Brookfield, Vt.

Pfister, G., P. G. Hess, L. K. Emmons, J.-F. Lamarque, C. Wiedinmyer, D. P. Edwards, G. Pétron, J. C. Gille, and G. W. Sachse (2005), Quantifying CO emissions from the 2004 Alaskan wildfires using MOPITT CO data, *Geophys. Res. Lett.*, *32*, L11809, doi:10.1029/2005GL022995.

Pickering, K. E., Y. Wang, W.-K. Tao, C. Price, and J.-F. Müller (1998), Vertical distributions of lightning NOx for use in regional and global chemical transport models, *J. Geophys. Res.*, *103*(D23), 31,203–31,216.

Pierce, R. B., et al. (2003), Regional Air Quality Modeling System (RAQMS) predictions of the tropospheric ozone budget over east Asia, *J. Geophys. Res.*, *108*(D21), 8825, doi:10.1029/2002JD003176.

Pierce, R. B., et al. (2007), Chemical data assimilation estimates of continental US ozone and nitrogen budgets during INTEX-A, *J. Geophys. Res.*, doi:10.1029/2006JD007722, in press.

Price, C., and J. Penner (1997), NOx from lightning: 1. Global distribution based on lightning physics, *J. Geophys. Res.*, *102*(D5), 5929–5941.

Sandu, A., D. Daescu, G. R. Carmichael, and T. Chai (2005), Adjoint sensitivity analysis of regional air quality models, *J. Comput. Phys.*, *204*(1), 222–252.

Stolarski, R. S., et al. (1995), 1995 Scientific Assessment of the atmospheric effects of stratospheric aircraft, *NASA Ref. Publ.*, 1381.

Streets, D. G., et al. (2003), An inventory of gaseous and primary aerosol emissions in Asia in the year 2000, *J. Geophys. Res.*, *108*(D21), 8809, doi:10.1029/2002JD003093.

Tang, Y., et al. (2003), Impacts of aerosols and clouds on photolysis frequencies and photochemistry during TRACE-P: 2. Three-dimensional study using a regional chemical transport model, *J. Geophys. Res.*, *108*(D21), 8822, doi:10.1029/2002JD003100.

Tang, Y., et al. (2004), Three-dimensional simulations of inorganic aerosol distributions in East Asia during spring 2001, *J. Geophys. Res.*, *109*, D19S23, doi:10.1029/2003JD004201.

Turquety, S., et al. (2007), Inventory of boreal fire emissions for North America in 2004: Importance of peat burning and pyroconvective injection, *J. Geophys. Res.*, *112*, D12S03, doi:10.1029/2006JD007281.

Winner, D. A., G. R. Cass, and R. A. Harley (1995), Effect of alternative boundary conditions on predicted ozone control strategy: A case study in Los Angeles area, *Atmos. Environ.*, *29*(33), 3451–3464.

J. A. Al-Saadi, M. A. Avery, R. B. Pierce, and G. W. Sachse, NASA Langley Research Center, Hampton, VA 23681, USA. (j.a.al-saadi@nasa.gov; m.a.avery@larc.nasa.gov; r.b.pierce@larc.nasa.gov; g.w.sachse@larc.nasa.gov)

E. L. Atlas, Rosenstiel School of Marine and Atmospheric Science, University of Miami, 4600 Rickenbacker Causeway, Miami, FL 33149, USA. (eatlas@rsmas.miami.edu)

W. H. Brune, Department of Meteorology, Pennsylvania State University, University Park, PA 16802, USA. (brune@ems.psu.edu)

G. R. Carmichael, T. Chai, and N. Thongboonchoo, Center for Global and Regional Environmental Research, University of Iowa, Iowa City, IA 52242, USA. (gcarmich@engineering.uiowa.edu; tchai@cgrer.uiowa.edu; nthongbo@cgrer.uiowa.edu)

J. E. Dibb, Institute for the Study of Earth, Oceans, and Space, University of New Hampshire, Durham, NH 03824, USA. (jack.dibb@unh.edu)

F. M. Flocke and G. Pfister, National Center for Atmospheric Research, Boulder, CO 80307, USA. (ffl@ucar.edu; pfister@ucar.edu)

J. S. Holloway and T. B. Ryerson, Chemical Sciences Division, Earth System Research Laboratory, NOAA, Boulder, CO 80305, USA. (john.s.holloway@noaa.gov; thomas.b.ryerson@noaa.gov)

L. W. Horowitz, Geophysical Fluid Dynamics Laboratory, NOAA, Princeton, NJ 08540, USA. (larry.horowitz@noaa.gov)

L. G. Huey and R. J. Weber, School of Earth and Atmospheric Sciences, Georgia Institute of Technology, Atlanta, GA 30332, USA. (greg.huey@eas.gatech.edu; rweber@eas.gatech.edu)

D. G. Streets, Argonne National Laboratory, Argonne, IL 60439, USA. (dstreets@anl.gov)

Y. Tang, Environmental Modeling Center, National Centers for Environmental Prediction, NOAA, W/NP22 Room 207, 5200 Auth Road, Camp Springs, MD 20746-4304, USA. (youhua.tang@noaa.gov)

J. M. Vukovich, Carolina Environmental Program, University of North Carolina, Chapel Hill, NC 27599, USA. (jeff_vukovich@unc.edu)